GLOBAL APPROACH TO THE SPECTRAL PROBLEM
OF MICROINSTABILITIES IN TOKAMAK PLASMAS
USING A GYROKINETIC MODEL

S. Brunner, M. Fivaz, T.M. Tran
& J. Vaclavik

Global Approach to the Spectral Problem of Microinstabilities in Tokamak Plasmas using a Gyrokinetic Model.

S.Brunner*, M.Fivaz, T.M.Tran and J. Vaclavik

Centre de Recherches en Physique des Plasmas, Association Euratom-Confédération Suisse,

Ecole Polytechnique Fédérale de Lausanne, CRPP-PPB, CH-1015 Lausanne, Switzerland

(June 4, 1998)

Abstract

Methods previously developed for a cylindrical system are generalized to a tokamak plasma for solving the full 2-dimensional eigenvalue problem of electrostatic microinstabilities in the frame of gyrokinetik theory. By solving the spectral problem in a special Fourier space adapted to the curved geometry, orbit width as well as Larmor radius can be kept to all orders. For a first numerical implementation, a large aspect ratio plasma with circular concentric magnetic surfaces is considered. A root finding algorithm for identifying the eigenfrequencies, based on a higher order Nyquist method, enables straightforward implementation on a parallel computer. Illustrative results of ITG (ion temperature gradient) -related instabilities are presented. These include scaling studies of the radial width, toroidicity and magnetic shear scans, as well as the effects of non-adiabatic trapped electron dynamics.

52.35.Kt, 52.25.Fi, 52.25.Dg, 52.35.-g

*E-mail: brunner@crppsun.epfl.ch

I. INTRODUCTION

The work presented in this paper is the generalization and application to a toroidal plasma of methods first developed for a cylindrical system [1] for solving the eigenvalue problem of microinstabilities in the frame of gyrokinetic theory. While most previous linear calculations have been carried out using the lowest order ballooning approximation [2]- local to a magnetic surface and limited to perturbations with high toroidal wave numbers- the approach presented here solves the full two-dimensional eigenmode structure in the poloidal plane. In particular, this allows one to cover the entire range from low to high toroidal wave numbers and to compute the radial extent of the instabilities, which provides valuable estimates for the radial correlation length.

The only previously published results from true global, eigenvalue studies were obtained using a code initially developed by Marchand, Tang and Rewoldt [3–5], which is based on a second order expansion with respect to the banana width and contains no finite Larmor radius (FLR) effects. This expansion leads to the presence of spurious modes in the spectra and therefore to the difficult identification of physical eigenmodes. The derivation presented here, based on solving the eigenvalue problem in a special Fourier space adapted to the toroidal geometry of the system, enables to keep orbit width as well as the Larmor radius to all orders and thus avoids the problem of non-physical modes. This formulation therefore stays consistent up to high toroidal wave numbers, i.e. short wavelengths.

Simultaneously to the development of this new eigenvalue code, another global, linear code was written, based on a time evolution, particle in cell (PIC) method [6,7]. These two complementary approaches have already allowed extensive benchmarking [8]. More comparisons will be presented in this paper.

In practice, solving the gyrokinetic equation (GKE) in the guiding center (GC) phase space of a tokamak plasma is numerically a costly process and therefore, possible implementation on a parallel computer is of great interest. For this, PIC codes are particularly adapted. It is shown here how an efficient root finding method [9], applied for identifying

the spectra of the system, also allows for a straightforward implementation of an eigenvalue code on a parallel machine.

In fact, in the past years, a limited number of global, non-linear PIC codes have been developed [10,11]. The main goal being to simulate anomalous transport in the turbulent state, these non-linear computations tend to be less accurate in the linear phase of the evolution. This defines a particularly interesting field for applying linear codes: determining global marginal stability over a wide parameter range [12].

In Sec.II a general derivation is given for the eigenvalue equation in a toroidal, axisymmetric system. At the present state, these results have been applied for numerical implementation to a large aspect ratio, low β plasma. The extensive modeling carried out in this simplified geometry is discussed in detail in Sec.III. Section IV provides some details on the numerical methods employed. Illustrative results are presented in Sec.V , including scans obtained by varying different parameters, such as the toroidal wave number, toroidicity and the magnetic shear. Scaling studies of the radial width, as well as non-adiabatic trapped electron effects are also discussed. More results can be found in reference [13]. Finally, conclusions are drawn in Sec.VI.

II. DERIVATION FOR A GENERAL AXISYMMETRIC SYSTEM

A. Starting Equations

The dynamics of each species is described by the GKE, appropriate for the low frequency microinstabilities. This equation, linearized for electrostatic perturbations, is given by [14]:

$$\frac{D}{Dt}\bigg|_{u.t.GC} \tilde{g}\,(\vec{R}, \mathcal{E}, \lambda, \sigma; t) = \left[\frac{\partial}{\partial t} + \vec{v}_{GC} \cdot \frac{\partial}{\partial \vec{R}}\right] \tilde{g} = -i\frac{q}{T}F_M(\omega - \omega^\star) < \phi >_g, \qquad (1)$$

where $D/Dt|u.t.GC$ stands for the total time derivative along the unperturbed trajectories of the GC. Through the gyro-averaged potential $< \phi >_g$, the GKE takes into account the Larmor radius to all orders.

3

For electrostatic microinstabilities, the system of equations may be closed by invoking quasineutrality:

$$\sum_{\text{species}} \tilde{\rho}_q\,(\vec{r},\omega) = 0, \tag{2}$$

where $\tilde{\rho}_q$ is the fluctuating part of the charge density for a given species.

In the above relations and in the following, we use the standard notations: ω the frequency of the perturbation, $\tilde{g}=\tilde{f}+q\phi F_M/T$ the non-adiabatic part of the fluctuating distribution function $\tilde{f}$, $F_M = N\exp(-\mathcal{E}/v_{th})^2/(2\pi v_{th}^2)^{3/2}$ the local Maxwellian distribution of equilibrium, q the electric charge, M the mass of the particle, $\Omega = qB/M$ the cyclotron frequency, $v_{th} = \sqrt{T/M}$ the thermal velocity, ϕ the electrostatic potential of the perturbation, $(\vec{r},\vec{v})$ the position of the particle in phase space, $\vec{R}=\vec{r}+(\vec{v}\times\vec{e}_{\parallel})/\Omega$ the guiding center position, $\mathcal{E} = v^2/2$ the kinetic energy, $\mu = v_\perp^2/2B$ the magnetic moment, $\lambda = B_0\mu/\mathcal{E}$ the "pitch-angle" variable, $\sigma = \text{sign}(v_{\parallel})$, $\vec{v}_{GC}= v_{\parallel}\,\vec{e}_{\parallel} + \vec{v}_d$ the GC velocity divided into parallel motion and magnetic drifts $\vec{v}_d= (1/\Omega)\,\vec{e}_{\parallel}\times\left[\left(v_\perp^2/2 + v_{\parallel}^2\right)\nabla\ln B + v_{\parallel}^2(\mu_0/B^2)\nabla p\right]$, p the plasma pressure. In an axisymmetric system, the magnetic field is of the form $\vec{B}= \nabla\psi\times\nabla\varphi + rB_\varphi\nabla\varphi$, (r,φ,z) being the cylindrical coordinates and ψ the poloidal magnetic flux. The amplitude of the magnetic field on the magnetic axis is given by B_0. Besides the parallel unit vector $\vec{e}_{\parallel}=\vec{B}/B$, one defines $\vec{e}_n= \nabla\psi/|\nabla\psi|$ and $\vec{e}_b=\vec{e}_{\parallel}\times\vec{e}_n$ (see Fig.1). In general $\nabla_\nu \equiv\vec{e}_\nu\cdot\nabla$. Density $N(\psi)$ and temperature $T(\psi)$ are flux functions, so that the diamagnetic drift frequency operator is given by $\omega^\star = (T/qB)\nabla_n\ln F_M(-i\nabla_b)$, with $\nabla_n\ln F_M = \nabla_n\ln N\left[1 + \eta(\mathcal{E}/v_{th}^2 - 3/2)\right]$ and $\eta = d\ln T/d\ln N$.

B. Solution to the GKE

Fourier representation appears naturally when solving the GKE, as it allows to perform explicitly integrations of the unknown potential ϕ. Indeed, by defining

$$\phi(\vec{r}) = \int d\vec{k}\; e^{i\vec{k}\cdot\vec{r}}\,\hat{\phi}\,(\vec{k}),$$

4

one can for instance carry out gyroaveraging:

$$
\begin{aligned}
<\phi>_g &= \int d\vec{k}\, e^{i\vec{k}\cdot\vec{R}}\, \overset{\wedge}{\phi}(\vec{k})\frac{1}{2\pi}\int_0^{2\pi} d\alpha \, \exp(-i\,\vec{k}\cdot\frac{\vec{v}\times\vec{e}_\parallel}{\Omega}) \\
&= \int d\vec{k}\, J_0\left(\frac{k_\perp v_\perp}{\Omega}\right) e^{i\vec{k}\cdot\vec{R}}\, \overset{\wedge}{\phi}(\vec{k}),
\end{aligned}
$$

where α is the gyroangle and J_0 the zero order Bessel function , containing FLR effects to all orders. As discussed in reference [1], it is practical to consider a wave decomposition more adapted to the geometry of the system than the standard plane wave representation. Thus, in this case, a toroidal wave decomposition is chosen, so that in fact one must read here:

$$
\int d\vec{k}\, e^{i\vec{k}\cdot\vec{r}}\, \overset{\wedge}{\phi}(\vec{k}) \longrightarrow \sum_{(k,m)} \overset{\wedge}{\phi}_{(k,m)} \exp i(\kappa\psi + m\chi + n\varphi), \tag{3}
$$

with (ψ, χ, φ) the magnetic coordinate system, which has been completed by a generalized poloidal angle χ, increasing by 2π over one poloidal rotation (see Fig.1). As the stationary state is axisymmetric, the toroidal wave number n can be fixed. However, the perturbation is generally a superposition of wave components with different sets of radial and poloidal wave numbers. Furthermore, as the mode structures are localized radially in an interval $[\psi_l, \psi_u]$, a Fourier series instead of a Fourier transform is also considered in this direction. Thus, the radial wave number takes the discrete values $\kappa = k2\pi/\Delta\psi$, where k is an integer and $\Delta\psi = |\psi_u - \psi_l|$. Note that for a given wave component, the wave vector $\vec{k}$ is now local:

$$
\vec{k} = \kappa\nabla\psi + m\nabla\chi + n\nabla\varphi. \tag{4}
$$

A problem arising with representation (3), when gyroaveraging near the magnetic axis, is pointed out and extensively discussed in reference [1]. To lighten notations, the symbol for plane wave representation will often be kept further on, although it will actually stand for the right hand side of (3).

The essential role of Fourier representation also appears when inverting the GKE for $\tilde{g}$ by integrating along the unperturbed GC trajectories:

$$
\begin{aligned}
\tilde{g}(\vec{R}, \mathcal{E}, \lambda, \sigma; \omega) = &-\int d\vec{k}\, e^{i\vec{k}\cdot\vec{R}}\, \overset{\wedge}{\phi}(\vec{k}) \times \\
&\int_{-\infty}^{t} dt' \frac{q}{T} F_M J_0(\frac{k_\perp v_\perp}{\Omega}) i(\omega - \omega^\star) \exp i\left[\vec{k}\cdot(\vec{R'}-\vec{R}) - \omega(t'-t)\right], \tag{5}
\end{aligned}
$$

5

having assumed Im $\omega > 0$, in agreement with causality, which ensures convergence of the time integral.

The GC trajectories $\vec{R}'\,(t')$ are given by the following differential equations and initial conditions:

$$\frac{d\vec{R}'}{dt'} = \vec{v}_{GC}\,(\vec{R}',\mathcal{E},\lambda,\sigma), \qquad \vec{R}'\,(t'=t) = \vec{R},$$

where $(\mathcal{E},\lambda)$ are invariants and σ changes its sign at the turning points in the case of trapped particles. As the system is axisymmetric, this differential equation must essentially be solved in the poloidal plane. The unperturbed system being time independent, the origin of time can be chosen arbitrarily when integrating along a given trajectory. In the following, this origin will be fixed as the particle passes $\chi = 0$, assuming that χ has been defined such that $|\,\vec{B}\,(\psi,\chi=0)| = B_{min}(\psi)$, where $B_{min}(\psi)$ (resp. $B_{max}(\psi)$) is the minimum (resp. maximum) of the magnetic field on a fixed magnetic surface $\psi =$const. With this definition, all particles, even the deeply trapped, pass at least one point in the poloidal plane where $\chi = 0$. Let us also define $\psi_0 = \psi'(t'=0)$, the magnetic surface on which the GC is located at $t' = 0$.

The time integral in (5) can somewhat be reduced, first by noting that the unperturbed distribution function F_M is invariant along the unperturbed trajectories. Furthermore, let us choose χ so that (ψ,χ,φ) becomes a straight field-line coordinate system [15]. For a wave component with fixed poloidal wave number m, the operator $\omega^\star$ then becomes a function of ψ and $\mathcal{E}$:

$$\omega^\star = \frac{T(\psi)}{q}\frac{\partial \ln F_M(\psi,\mathcal{E})}{\partial \psi}\frac{m}{q_s(\psi)},$$

where $q_s(\psi)$ is the safety factor profile. The variation of $\omega^\star$ over the unperturbed trajectories, of order $\delta\psi$, i.e. due to drifts, can therefore be neglected to lowest order in the gyro-ordering parameter $\epsilon = \lambda_L/a$ (λ_L is the ion Larmor radius and a a characteristic length of equilibrium such as the minor radius of the plasma). In the same way, temperature $T(\psi)$ alone is considered invariant. Finally, the argument $k_\perp v_\perp/\Omega$ of the Bessel function varies on the

order of the inverse aspect ratio and in practice a ψ-surface averaged value $< k_\perp v_\perp/\Omega >_\psi$ is considered. Thus, relation (5) becomes:

$$\tilde{g} = -\frac{q}{T} F_M \int d\vec{k} \; J_0(\frac{k_\perp v_\perp}{\Omega}) e^{i\vec{k}\cdot\vec{R}} \overset{\wedge}{\phi} (\vec{k}) i(\omega - \omega^\star)\mathcal{P}. \tag{6}$$

The key term in (6) is the propagator:

$$\mathcal{P}(\vec{R}, \vec{k}, \mathcal{E}, \lambda, \sigma; \omega) = \int_{-\infty}^{t} dt' \exp i \left[\vec{k} \cdot (\vec{R'} - \vec{R}) - \omega(t' - t)\right], \tag{7}$$

which is the time integral of the phase factor of a given wave component.

Let us further develop $\mathcal{P}$ in the case of a toroidal system, so that the resonances it contains appear explicitly. This is particularly useful for numerical implementation, as it allows to discard all but the leading contributions. To start, note that in (7) the phase

$$\vec{k} \cdot (\vec{R'} - \vec{R}) = \int_t^{t'} dt'' \; \vec{k} \cdot \vec{v}_{GC} (\vec{R'}, \mathcal{E}, \lambda, \sigma), \tag{8}$$

is usually not periodic in time. Indeed, although the axisymmetry of the system leads to a periodic trajectory in the poloidal plane, the toroidal motion, being the integral of a periodic function, in general contains a secular term:

$$\varphi'(t' + \tau_\nu) - \varphi'(t') = \int_{t'}^{t'+\tau_\nu} dt'' \nabla\varphi \cdot \vec{v}_{GC} = <\dot{\varphi}> \tau_\nu,$$

where τ_ν is the time period in the poloidal plane and $<\dot{\varphi}>$ the average toroidal angular velocity, corresponding to the precessional drift $<\dot{\varphi}>_b$ in the case of trapped particles. In fact, $\chi'(t')$ also contains a secular term for trajectories enclosing the magnetic axis, which however does not affect the periodicity of the phase factor $\exp i \left[\vec{k} \cdot (\vec{R'} - \vec{R})\right]$ itself:

$$\chi'(t' + \tau_\nu) - \chi'(t') = \int_{t'}^{t'+\tau_\nu} dt'' \nabla\chi \cdot \vec{v}_{GC} = \pm 2\pi, \qquad \text{if magnetic axis is encircled.}$$

Thus, by subtracting the toroidal secular term in the phase, the following function becomes periodic and can therefore be decomposed into a Fourier series [16]:

$$\exp i \int_0^t dt' (\vec{k} \cdot \vec{v}_{GC} - n <\dot{\varphi}>) = \sum_{p=-\infty}^{+\infty} C_p \exp ip\omega_\nu t$$

$$\Longleftrightarrow \tag{9}$$

$$C_p(k, m; \psi_0, \mathcal{E}, \lambda(, \sigma)) = \frac{1}{\tau_\nu} \int_0^{\tau_\nu} dt \exp i \left[\int_0^t dt' (\vec{k} \cdot \vec{v}_{GC} - n <\dot{\varphi}>) - p\omega_\nu t\right],$$

where $\omega_\nu = 2\pi/\tau_\nu$ is the frequency of the motion in the poloidal plane, corresponding to the transit frequency ω_t (resp. bounce frequency ω_b) in the case of circulating (resp. trapped) particles. For circulating particles, the coefficients C_p are still function of $\sigma = \text{sign}(v_\parallel)$, for trapped particles however both $\sigma = \pm 1$ are covered on the same trajectory. With the above decomposition, the time integration in (7) can be carried out analytically:

$$
\begin{aligned}
\mathcal{P} &= \exp\left[-i\int_0^t dt''(\vec{k}\cdot\vec{v}_{GC} - \omega)\right]\int_{-\infty}^t dt' \sum_p C_p \exp i(p\omega_\nu + n <\dot{\varphi}> -\omega)t' \\
&= \exp\left[-i\int_0^t dt''(\vec{k}\cdot\vec{v}_{GC} - n <\dot{\varphi}>)\right]\sum_{p=-\infty}^{+\infty} \frac{C_p\, e^{ip\omega_\nu t}}{i(p\omega_\nu + n <\dot{\varphi}> -\omega)}.
\end{aligned}
\tag{10}
$$

The possible resonances relative to the basic frequency ω_ν and its harmonics now appear explicitly.

The perturbed charge density $\tilde{\rho}_q$ is evaluated from $\tilde{f} = -q\phi F_M/T + \tilde{g}$ by integrating over velocity space, after transforming back to particle variables, which basically consists in replacing $\exp i\,\vec{k}\vec{R}$ in Eq.(6) by $\exp i\,\vec{k}\cdot\left[\vec{r} + (\vec{v}\times\vec{e}_\parallel)/\Omega\right]$:

$$
\tilde{\rho}_q(\vec{r}) = -\frac{Nq^2}{T}\left[\phi + \int d\vec{k}\, e^{i\vec{k}\cdot\vec{r}} \hat{\phi}(\vec{k})\int d\vec{v}\, J_0^2(\frac{k_\perp v_\perp}{\Omega})\frac{F_M}{N}i(\omega - \omega^\star)\mathcal{P}\right].
\tag{11}
$$

In (11) the gyroangle integration has again been performed, providing a second Bessel function J_0, so that $\int d\vec{v}$ stands for

$$
\int d\vec{v} \equiv 2\pi\int_0^{+\infty} v_\perp dv_\perp\int_{-\infty}^{+\infty} dv_\parallel = 2\pi\frac{B(\vec{r})}{B_0}\sum_{\sigma=\pm 1}\int_0^{+\infty}\mathcal{E}d\mathcal{E}\int_0^{B_0/B(\vec{r})}\frac{d\lambda}{|v_\parallel|}.
\tag{12}
$$

The quasineutrality relation (2), which leads to the final eigenvalue equation, is ultimately solved in the special toroidal Fourier representation defined in (3). The perturbed charge density $\tilde{\rho}_q$ is therefore projected on $\exp i\,\vec{k}\cdot\vec{r}$, giving:

$$
\tilde{\rho}_q(\vec{k}) = \int d\vec{r}\, e^{-i\vec{k}\cdot\vec{r}}\,\tilde{\rho}_q(\vec{r}) = \int d\vec{k'}\, M(\vec{k},\vec{k'})\hat{\phi}(\vec{k'}),
\tag{13}
$$

the kernel of this integral relation being given by:

$$
M(\vec{k},\vec{k'}) = \int d\vec{r}\, e^{-i(\vec{k}-\vec{k'})\cdot\vec{r}}\left(-\frac{Nq^2}{T}\right)\left[1 + \int d\vec{v}\, J_0^2(\frac{k'_\perp v_\perp}{\Omega})\frac{F_M}{N}i(\omega - \omega^\star)\mathcal{P}\right].
\tag{14}
$$

Concerning notations, $\vec{k}$ stands for the set of mode numbers (k, m, n), while $\vec{k'}$ stands for the set (k', m', n). All terms tagged with a prime, such as $\omega^{*'}$, are evaluated for $\vec{k'}$. Furthermore, in (14), $\int d\,\vec{r}$ symbolically represents:

$$\int d\,\vec{r} \equiv \frac{1}{\Delta\psi} \frac{1}{(2\pi)^2} \int_{\psi_l}^{\psi_u} d\psi \int_{-\pi}^{\pi} d\chi \int_{-\pi}^{\pi} d\varphi\, \mathcal{J},$$

with $\mathcal{J}^{-1} = \nabla\psi \cdot (\nabla\chi \times \nabla\varphi)$ the Jacobian of the magnetic coordinate system.

A certain number of operations are still carried out, allowing to cast relation (14) into an elegant form. When performing the integral $\int d\,\vec{r} \int d\,\vec{v}$ over phase space to evaluate the non-adiabatic contribution to $M(\vec{k}, \vec{k'})$, one starts by interchanging the integrals relative to χ and λ:

$$\int_{-\pi}^{\pi} d\chi \int_{0}^{B_0/B(\psi,\chi)} d\lambda = \int_{0}^{B_0/B_{min}(\psi)} d\lambda \int_{\chi_l}^{\chi_u} d\chi,$$

with

$$\chi_{l,u} = \pm\pi \quad \text{if} \quad 0 < \lambda < \frac{B_0}{B_{max}(\psi)} \quad : \text{circulating particles}$$

$$\frac{B(\psi, \chi_{l,u})}{B_0} = \frac{1}{\lambda} \quad \text{if} \quad \frac{B_0}{B_{max}(\psi)} < \lambda < \frac{B_0}{B_{min}(\psi)} \quad : \text{trapped particles.}$$

Then, the following change of variables is carried out:

$$(\psi, \chi) \longleftrightarrow (\psi_0, t), \tag{15}$$

which, for fixed $(\mathcal{E}, \lambda)$, is based on the above defined trajectories:

$$\psi(\psi_0, t) = \psi_0 + \int_{0}^{t} dt'' \nabla\psi \cdot \vec{v}_{GC} = \psi_0 + \mathcal{O}(\epsilon), \tag{16}$$

$$\chi(\psi_0, t) = \int_{0}^{t} dt'' \nabla\chi \cdot \vec{v}_{GC} = -\int_{0}^{t} dt'' \frac{v_{\parallel}}{\mathcal{J}B} + \mathcal{O}(\epsilon). \tag{17}$$

To lowest order in the gyro-ordering parameter ϵ, the Jacobian of transformation (15) is therefore given by:

$$d\psi d\chi = \left| \frac{D(\psi, \chi)}{D(\psi_0, t)} \right| d\psi_0 dt = \frac{|v_{\parallel}|}{\mathcal{J}B} d\psi_0 dt.$$

This leads to the relation:

9

$$\sum_{\sigma=\pm 1} \int_{\chi_l}^{\chi_u} d\chi = \overset{\sim}{\sum_{\sigma=\pm 1}} \int_0^{\tau_\nu} \frac{|v_\parallel|}{\mathcal{J}B} dt,$$

where $\overset{\sim}{\sum}_{\sigma=\pm 1}$ is only carried out for circulating particles. In fact, in the same way as (6) was established, the difference between ψ and ψ_0, of order $\mathcal{O}(\epsilon)$, is only taken into account in the phase factor and to lighten notations, ψ_0 is ultimately replaced again by ψ. In this way, one finally obtains:

$$M(\vec{k}, \vec{k'}) \equiv M_{(k,m),(k',m')} = \frac{1}{\Delta\psi} \int_{\psi_l}^{\psi_u} d\psi e^{-i(\kappa-\kappa')\psi} \left(-\frac{Nq^2}{T}\right) \left[\frac{1}{2\pi} \int_{-\pi}^{\pi} \mathcal{J} d\chi e^{-i(m-m')\chi} + \right.$$

$$\frac{1}{B_0} \overset{\sim}{\sum_{\sigma=\pm 1}} \int_0^{+\infty} d\mathcal{E}\, \mathcal{E} \int_0^{B_0/B_{min}} d\lambda\, J_0^2(\frac{k'_\perp v_\perp}{\Omega}) \frac{F_M}{N} i(\omega - \omega^{*\prime}) \times \tag{18}$$

$$\int_0^{\tau_\nu} dt \exp\left\{-i \int_0^t dt'' [(\kappa - \kappa')\nabla\psi + (m - m')\nabla\chi] \cdot \vec{v}_{GC}\right\} \mathcal{P}\bigg]$$

$$= \frac{1}{\Delta\psi} \int_{\psi_l}^{\psi_u} d\psi e^{-i(\kappa-\kappa')\psi} \left(-\frac{Nq^2}{T}\right) \left[\frac{1}{2\pi} \int_{-\pi}^{\pi} \mathcal{J} d\chi e^{-i(m-m')\chi} + \right. \tag{19}$$

$$\left. \frac{1}{B_0} \overset{\sim}{\sum_{\sigma=\pm 1}} \int_0^{+\infty} d\mathcal{E}\, \mathcal{E} \frac{F_M}{N}(\omega - \omega^{*\prime}) \int_0^{B_0/B_{min}} d\lambda J_0^2(\frac{k'_\perp v_\perp}{\Omega}) \tau_\nu \sum_{p=-\infty}^{+\infty} \frac{C_p^*(\vec{k})C_p(\vec{k'})}{p\omega_\nu + n <\dot{\varphi}> -\omega} \right],$$

having used relation (10) for $\mathcal{P}$ and definition (9) for the coefficients C_p. The notation $*$ stands for the complex conjugate.

C. Eigenvalue equation in Fourier representation

The quasineutrality equation constitutes the actual eigenvalue equation. Written in Fourier representation, equation (2) reads:

$$\sum_{\text{species}} \overset{\wedge}{\overset{\sim}{\rho}_q} (\vec{k}, \omega) = \sum_{\vec{k'}} M^{tot}_{\vec{k}, \vec{k'}}(\omega) \overset{\wedge}{\phi_{\vec{k'}}} = 0, \tag{20}$$

where M^{tot} is the sum over all species of contributions of the form (19):

$$M^{tot} = \sum_{\text{species}} M.$$

Relation (20) is not a standard eigenvalue problem, as $M^{tot}(\omega)$ is an intricate function of ω. One can nonetheless always write the characteristic equation for the eigenfrequencies:

$$\det M^{tot}(\omega) = 0, \qquad (21)$$

$\det M^{tot}$ being the determinant of the matrix.

The main advantage of solving the eigenvalue equation in Fourier representation, lies in the fact that there is no singularity to be integrated, as the one which appears when solving the integral eigenvalue equation obtained in configuration space. This is related to the fact that in Fourier representation, the system is already naturally discretized by the wave numbers (k, m) taking integer values. More details to this point are given in reference [1].

III. LARGE ASPECT RATIO TOKAMAK

For numerical implementation, the above relations have been applied to a large aspect ratio tokamak. In this case, the plasma is confined by a magnetic field of the form:

$$\vec{B} = B_0 \frac{R}{r} \left(-\frac{\rho}{Rq_s} \vec{e_\theta} + \vec{e_\varphi} \right), \qquad (22)$$

where R is the major radius and $q_s(\rho)$ an arbitrary safety factor profile. The standard toroidal coordinates (ρ, θ, φ) are considered here, which in this large aspect ratio configuration define a straight field line system. For a fixed toroidal wave component, the local wave vector (4) is now given by

$$\vec{k} = k_\rho \vec{e_\rho} + k_\theta \vec{e_\theta} + k_\varphi \vec{e_\varphi},$$

where $k_\rho = k2\pi/\Delta\rho$, $k_\theta = m/\rho$ and $k_\varphi = n/R$, $\Delta\rho = |\rho_u - \rho_l|$ being the width of the radial interval $[\rho_l, \rho_u]$ considered.

Applying the large aspect ratio approximation, only lowest order non-vanishing terms with respect to the inverse aspect ratio $A^{-1} = \rho/R$ are retained. In this way, together with a set of other approximations, the large aspect ratio geometry allows one to push the analytical derivation further than in a general tokamak geometry and therefore leads to the simplest possible equations for a first numerical implementation.

A convenient parameter for the subsequent expressions, especially when treating trapped particles, is given by

$$X = \frac{1 - \lambda B_{min}/B_0}{2\lambda A^{-1}}, \tag{23}$$

allowing one, as λ, to classify the two sub-groups of particles:

circulating: $\qquad 0 < \lambda < \dfrac{B_0}{B_{max}} \Longleftrightarrow 1 < X < +\infty,$

trapped: $\qquad \dfrac{B_0}{B_{max}} < \lambda < \dfrac{B_0}{B} < \dfrac{B_0}{B_{min}} \Longleftrightarrow 0 < \sin^2 \dfrac{\theta}{2} < X < 1,$

with $B_{max,min} = B_0(1 \pm A^{-1})$ and $B = B_0(1 - A^{-1}\cos\theta)$ the magnetic field at the point of interest (ρ, θ).

In the following, contributions of the form (19) are derived successively for circulating ions, trapped ions and trapped electrons. To lighten notations, subscripts characterizing physical quantities of different species are usually omitted.

A. Circulating ions

For this fraction of particles, the modulation of $v_{\parallel}$ and $v_{\perp}$ along a given trajectory, due to the variation of $| \vec{B} |$, is neglected, so that in fact all particles are approximated as highly passing. The only toroidal effect which is retained are the GC drifts, which for the low pressure equilibrium defined above are vertical:

$$\vec{v}_d = v_{dz}\, \vec{e}_z = \frac{1}{\Omega R}\left(\frac{v_{\perp}^2}{2} + v_{\parallel}^2\right) \vec{e}_z \ .$$

In the absence of drifts, the motion parallel to the magnetic field leads to a circular trajectory in the poloidal plane:

$$\rho'(t') = \rho = \text{const}, \tag{24}$$

$$\theta'(t') = -\omega_t t', \tag{25}$$

with $\omega_t = v_{\parallel}/Rq_s$ the transit frequency. Drifts are then taken into account iteratively by integrating their contribution along the lowest order trajectory (25) when evaluating the phase (8):

12

$$\int_0^t dt' \; \vec{k} \cdot \vec{v}_{GC} = k_\parallel v_\parallel t + \int_0^t dt' \; \vec{k} \cdot \vec{v}_d = k_\parallel v_\parallel t - \int_0^t dt' k_\perp v_{dz} \cos(\theta' + \beta_t)$$

$$= k_\parallel v_\parallel t + x_t \left[\sin(\theta' + \beta_t) - \sin \beta_t \right], \qquad (26)$$

having used

$$k_z = -(k_\rho \sin\theta + k_\theta \cos\theta) = -k_\perp \cos(\theta + \beta_t),$$

and the definitions:

$$x_t(\vec{k}) = k_\perp v_{dz}/\omega_t,$$

$$\cos\beta_t(\vec{k}) = \frac{k_\theta}{k_\perp} \quad \text{and} \quad \sin\beta_t(\vec{k}) = -\frac{k_\rho}{k_\perp}.$$

The component of $\vec{k}$ parallel and perpendicular to the magnetic field are approximated by

$$k_\parallel = (nq_s - m)/Rq_s, \qquad k_\perp = \sqrt{k_\rho^2 + k_\theta^2}.$$

From (26) one obtains $<\dot{\varphi}> = v_\parallel/R$, so that the Fourier coefficients of the harmonic decomposition (9) become:

$$C_p(k, m; \rho, v_\parallel, v_\perp) = \frac{1}{\tau_t} \int_0^{\tau_t} dt \exp i \left\{ -m\omega_t t + x_t \left[\sin(-\omega_t t + \beta_t) - \sin\beta_t \right] - p\omega_t t \right\}$$

$$= J_{-(p+m)}(x_t) \exp i \left[\frac{k_\rho v_{dz}}{\omega_t} - (p+m)\beta_t \right], \qquad (27)$$

where J stands again for the Bessel function.

Inserting (27) into (19) provides the contribution to the eigenvalue equation from circulating ions:

$$M_{(k,m),(k',m')}^{circ.ions} = \frac{1}{\Delta\rho} \int_{\rho_l}^{\rho_u} d\rho \, e^{-i(k_\rho - k'_\rho)\rho} \left(-\frac{Rq_s}{B_0} \frac{Nq^2}{T} \right) \left[\alpha_t \delta_{m,m'} + \right.$$

$$e^{i(m\beta_t - m'\beta'_t)} \int_{circ.} d\vec{v} \, \frac{F_M}{N} (\omega - \omega^{*'}) J_0^2(x'_L) \times \qquad (28)$$

$$\left. \sum_{p=-\infty}^{+\infty} \frac{J_{-(p+m)}(x_t) J_{-(p+m')}(x'_t) e^{ip(\beta_t - \beta'_t)}}{(p + nq_s)\omega_t - \omega} \right],$$

having used $\mathcal{J} = Rq_s/B_0$ and the notation $\delta_{m,m'}$ for the Kronecker relation as well as $x_L = k_\perp v_\perp/\Omega$. The adiabatic term in (28) has been weighted by the fraction α_t of circulating ions.

Neglecting all drifts in transformation (15), applied when going from (18) to (19), corresponds to replacing $\beta_t \equiv \beta_t(\vec{k})$ by $\beta_t' \equiv \beta_t(\vec{k'})$ as well as $x_t \equiv x_t(\vec{k})$ by $x_t' \equiv x_t(\vec{k'})$ in (28), leading to an even simpler relation:

$$M^{circ.ions}_{(k,m),(k',m')} = \frac{1}{\Delta\rho}\int_{\rho_l}^{\rho_u} d\rho\, e^{-i(k_\rho - k'_\rho)\rho}\left(-\frac{Rq_s}{B_0}\frac{Nq^2}{T}\right)[\alpha_t \delta_{m,m'} +$$

$$e^{i(m-m')\beta_t'}\int_{circ.} d\,\vec{v}\,\frac{F_M}{N}(\omega - \omega^{\star'})J_0^2(x'_L)\sum_{p=-\infty}^{+\infty}\frac{J_p(x'_t)J_{(p-m+m')}(x'_t)}{k'_\parallel v_\parallel - p\omega_t - \omega}\Bigg], \quad (29)$$

having also carried out the transformation $p \longrightarrow -(p+m')$. In the approximation of highly passing ions, it is practical to come back to the velocity variables $(v_\parallel, v_\perp)$. The magnetic surface-average boundary condition (evaluated at $\theta = \pm\pi/2$) for circulating particles in velocity space is then given by:

$$v_\parallel > \sqrt{B_{max}/B_0 - 1}\ v_\perp \quad : \text{circulating.}$$

Concerning the velocity dependence of the different terms in (29), let us recall that $F_M \sim \exp -(v_\parallel^2 + v_\perp^2)/2$, $\omega^\star \sim 1 + \eta(v_\perp^2 + v_\parallel^2 - 3)/2$, $x_L \sim v_\perp$, $x_t \sim (v_\perp^2/2 + v_\parallel^2)/v_\parallel$ and $\omega_t \sim v_\parallel$. Thus, the resonant denominator is not a function of $v_\perp$, so that the integrals with respect to this variable can be precalculated numerically, independently of the unknown frequency ω. In terms of the normalized velocity $\vec{v} = \vec{v}/v_{th}$, these integrals are of the form:

$$I^j_{v_\perp}(\rho, \tilde{k}_\perp, v_\parallel, p, p') = \int_0^{v_\parallel/\sqrt{A^{-1}}} dv_\perp v_\perp^{2j+1} e^{-v_\perp^2/2} J_0^2(\tilde{k}_\perp v_\perp)J_p(x_t)J_{p'}(x_t), \quad j = 0, 1,$$

$$\text{with}\quad x_t = \frac{\tilde{k}_\perp q_s}{v_\parallel}\left(\frac{v_\perp^2}{2} + v_\parallel^2\right)\quad \text{and}\quad \tilde{k}_\perp = k_\perp v_{th}/\Omega.$$

The resonant denominators are however function of $v_\parallel$, so that the integral with respect to this variable must be recalculated numerically for each frequency ω. The final form for numerical implementation therefore reads:

$$M^{circ.ions}_{(k,m),(k',m')} = \frac{1}{\Delta\rho}\int_{\rho_l}^{\rho_u} d\rho\, e^{-i(k_\rho - k'_\rho)\rho}\left(-\frac{Rq_s}{B_0}\frac{Nq^2}{T}\right)\Bigg[\alpha_t\delta_{m,m'} + e^{i(m-m')\beta_t'}\frac{1}{\sqrt{2\pi}}\int_0^{+\infty} dv_\parallel e^{-v_\parallel^2/2} \times$$

$$\sum_{p=-\infty}^{+\infty}\frac{\left\{\omega - \omega'_N\left[1 + \eta(v_\parallel^2 - 3)/2\right]\right\}I^0_{v_\perp}(p,p') - \omega'_N\eta I^1_{v_\perp}(p,p')/2}{k'_\parallel v_{th}v_\parallel - p\omega_t - \omega}\Bigg]\Bigg|_{p'=p-m+m'}, \quad (30)$$

having used the notation $\omega_N = (Tk_\theta/qB)d\ln N/d\rho$.

14

B. Trapped ions

While $\mid \vec{B} \mid$ had been considered flat in the case of circulating ions, it is approximated by a harmonic well in the case of trapped ions, i.e. $\mid \vec{B} \mid$ is expanded to second order around $\theta = 0$, where the field is minimum:

$$B \simeq B_{min} + B_0 A^{-1} \frac{1}{2} \theta^2.$$

In other terms, all trapped ions are approximated as deeply trapped. Thus, the spirit of the following derivation is to assume $X \ll 1$ (see definition (23)), the final expression being then applied for all values of X: $0 < X < 1$. As for the barely passing particles in the highly passing approximation, the barely trapped particles are not described correctly with this model. However, the effect of these marginal particles should not be dominant, this will be confirmed by the numerical results in section V.

The lowest order motion along the magnetic field is easily obtained starting from the conservation of kinetic energy:

$$\mathcal{E} = \frac{1}{2} v_{\parallel}^2 + B \mu \simeq \frac{1}{2} (R q_s \frac{d\theta}{dt})^2 + (B_{min} + B_0 A^{-1} \frac{1}{2} \theta^2) \mu,$$

leading to

$$\frac{\mathcal{E}(1 - \lambda B_{min}/B_0)}{(R q_s)^2} \simeq 2 \omega_b^2 X = \frac{1}{2} (\frac{d\theta}{dt})^2 + \frac{1}{2} \omega_b^2 \theta^2, \tag{31}$$

having used $\lambda \simeq (B_0/B_{min})(1 - 2A^{-1} X B_0/B_{min}) + \mathcal{O}(X^2)$ and the expression for the bounce frequency:

$$\omega_b = \frac{\sqrt{A^{-1} \mathcal{E}}}{R q_s}.$$

By analogy with the energy conservation of a harmonic oscillator, one can immediately establish from (31) the lowest order motion along θ for deeply trapped particles:

$$\rho'(t') = \rho = \text{const}, \tag{32}$$

$$\theta'(t') = \theta_b \sin(\omega_b t'), \tag{33}$$

15

with the turning point angle being given by

$$\theta_b = 2\sqrt{X}.$$

The radial motion, due to drifts, is again evaluated iteratively by integration along the lowest order trajectory (33):

$$\rho'(t') - \rho'(t=0) = \int_0^{t'} dt'' \nabla \rho \cdot \vec{v}_{GC} = -\int_0^{t'} dt'' \sin\theta'' v_{dz} = -\frac{\mathcal{E}}{\Omega R} \int_0^{t'} dt'' \theta_b \sin\omega_b t''$$

$$= \rho_b[\cos(\omega_b t') - 1] = -2\rho_b \sin^2(\frac{\omega_b t'}{2}), \tag{34}$$

having applied $\vec{e}_\rho \cdot \vec{e}_z = -\sin\theta \simeq -\theta$ as well as $v_{dz} \simeq \mathcal{E}/\Omega R$ and using the relation for the half banana width:

$$\rho_b = \frac{2q_s}{\Omega} \sqrt{\frac{\mathcal{E}X}{A^{-1}}}.$$

The motion in the toroidal direction is the superposition of the oscillation along the magnetic field line and the precessional drift $<\dot{\varphi}>_b$:

$$\varphi'(t') - \varphi'(t'=0) = \int_0^{t'} dt'' \nabla\varphi \cdot \vec{v}_{GC} = -q_s\theta'(t') + <\dot{\varphi}>_b t'. \tag{35}$$

The toroidal precessional drift is the combined effect of the parallel motion along the magnetic field line and the vertical drifts $\vec{v}_d$. Therefore, to obtain $<\dot{\varphi}>_b$, one cannot proceed iteratively, as these two motions must be treated simultaneously. The derivation of $<\dot{\varphi}>_b$, for the large aspect ratio geometry considered here, is given in Ref. [17]:

$$<\dot{\varphi}>_b = -\frac{\mathcal{E}}{R^2\Omega} \frac{q_s}{A^{-1}} G, \tag{36}$$

$$G(\rho, X) = 4\lambda \left\{ \hat{s} \left[(X-1) + \frac{E(X)}{K(X)} \right] + \frac{1}{2} \left[\frac{E(X)}{K(X)} - \frac{1}{2} \right] \right\}, \tag{37}$$

where $K(X)$ and $E(X)$ are the complete elliptic integrals of the first and second kind respectively (using definitions from Ref. [18]) and $\hat{s} = d\ln q_s/d\ln\rho$ is the magnetic shear. Relation (37) for the factor G is valid for $0 < X < 1$. Instead of taking the deeply trapped limit $X \ll 1$, a single X-averaged value $<G>_X$ for each magnetic surface ρ is considered. The advantage of this procedure is twofold. First, as will be shown, it enables to perform

16

part of the final velocity integrals analytically. Second, it allows one to take into account the contribution of both, the deeply and less deeply trapped particles, whose toroidal drift tend to be in opposite directions. In this respect, the modeling goes somewhat beyond the deeply trapped particle approximation. The average of G is taken at $\theta = 0$, the point reached by all trapped particles:

$$
\begin{aligned}
< G >_X (\rho) &= \left(\int_{trap.} d^3 v \, F_M \right)^{-1} \int_{trap.} d^3 v \, F_M \, G \\
&= \frac{B_{min}}{B_0} \frac{A^{-1}}{\sqrt{1 - B_{min}/B_{max}}} \int_0^1 dX \frac{\lambda^2}{\sqrt{1 - \lambda B_{min}/B_0}} G(\rho, X),
\end{aligned} \tag{38}
$$

having used Rel.(12) together with $d\lambda/dX = -2A^{-1}\lambda^2$. The above integral is ultimately evaluated numerically.

The full phase factor is obtained by combining relations(33), (34) and (35):

$$
\begin{aligned}
\int_0^t dt' \, \vec{k} \cdot \vec{v}_{GC} &= (m - nq_s)\theta_b \sin \omega_b t + k_\rho \rho_b (\cos \omega_b t - 1) + n <\dot{\varphi}>_b t \\
&= x_b \sin(\omega_b t + \beta_b) - k_\rho \rho_b + n <\dot{\varphi}>_b t,
\end{aligned}
$$

with

$$
x_b(\vec{k}) = \sqrt{(m - nq_s)^2 \theta_b^2 + (k_\rho \rho_b)^2},
$$

$$
\cos \beta_b(\vec{k}) = \frac{(m - nq_s)\theta_b}{x_b} \quad \text{and} \quad \sin \beta_b(\vec{k}) = \frac{k_\rho \rho_b}{x_b}.
$$

The Fourier coefficients (9) of the harmonic decomposition can now be evaluated:

$$
\begin{aligned}
C_p(k, m; \rho, \mathcal{E}, X) &= \frac{1}{\tau_b} \int_0^{\tau_b} dt \exp i \left[x_b \sin(\omega_b t + \beta_b) - k_\rho \rho_b - p \omega_b t \right] \\
&= J_p(x_b) \exp i(p\beta_b - k_\rho \rho_b).
\end{aligned} \tag{39}
$$

Inserting (39) into (19) gives the contribution to the eigenvalue equation from trapped ions:

$$
\begin{aligned}
M^{trap.ions}_{(k,m),(k',m')} = \frac{1}{\Delta\rho} \int_{\rho_l}^{\rho_u} d\rho \, e^{-i(k_\rho - k'_\rho)\rho} \left(-\frac{Rq_s}{B_0} \frac{Nq^2}{T} \right) \Big[\alpha_b \delta_{m,m'} + \\
\sqrt{\frac{2A^{-1}}{\pi}} \int_0^{+\infty} \frac{d\mathcal{E} \sqrt{\mathcal{E}}}{v_{th}^3} e^{-\mathcal{E}/v_{th}^2} (\omega - \omega^{\star'}) J_0^2(x'_L) \times \\
\int_0^1 dX \sum_{p=-\infty}^{+\infty} \frac{J_p(x_b) J_p(x'_b) e^{ip(\beta_b - \beta'_b)}}{n <\dot{\varphi}>_b - p\omega_b - \omega} \Big],
\end{aligned} \tag{40}
$$

having taken the approximation $x_L = k_\perp \sqrt{2\mathcal{E}}/\Omega$, which is justified for trapped particles and transformed $p \longrightarrow -p$. In (40), the adiabatic term has been weighted by the fraction α_b of trapped particles (naturally $\alpha_t + \alpha_b = 1$). Considering in (40), as already discussed above, an X-averaged relation for $<\dot{\varphi}>_b$, the integrals with respect to X reduce to:

$$I_X(\tilde{x}_b, \tilde{x}_b{}', p) = \int_0^1 dX J_p(x_b) J_p(x_b') = \int_0^1 dX J_p(\sqrt{X}\ \tilde{x}_b) J_p(\sqrt{X}\ \tilde{x}_b{}'),$$

with

$$\tilde{x}_b\ (k, m; \rho, \mathcal{E}) = 2\sqrt{(m - nq_s)^2 + \left(\frac{q_s k_\rho}{\Omega}\right)^2 \frac{\mathcal{E}}{A^{-1}}}.$$

These integrals can be carried out analytically [19]:

$$I_X(\tilde{x}_b, \tilde{x}_b{}', p) = 2\frac{\tilde{x}_b\ J_{p-1}(\tilde{x}_b) J_p(\tilde{x}_b{}') - \tilde{x}_b{}'\ J_p(\tilde{x}_b) J_{p-1}(\tilde{x}_b{}')}{\tilde{x}_b{}'^2 - \tilde{x}_b{}^2} \quad \text{if} \quad \tilde{x}_b{}' \neq \tilde{x}_b,$$

$$I_X(\tilde{x}_b, \tilde{x}_b{}', p) = J_p^2(\tilde{x}_b) - J_{p-1}(\tilde{x}_b) J_{p+1}(\tilde{x}_b) \quad \text{if} \quad \tilde{x}_b{}' = \tilde{x}_b\ .$$

Note however that the resonant denominators remain functions of $\mathcal{E}$, as $\omega_b \sim \sqrt{\mathcal{E}}$ and $<\dot{\varphi}>_b \sim \mathcal{E}$. The integrals with respect to this variable must therefore be recalculated numerically for each frequency ω. The final form for numerical implementation thus reads:

$$M_{(k,m),(k',m')}^{trap.ions} = \frac{1}{\Delta\rho} \int_{\rho_l}^{\rho_u} d\rho e^{-i(k_\rho - k_\rho')\rho} \left(-\frac{Rq_s}{B_0} \frac{Nq^2}{T}\right) \left[\alpha_b \delta_{m,m'} + \sqrt{\frac{2A^{-1}}{\pi}} \int_0^{+\infty} dE\sqrt{E} e^{-E} \times \right.$$

$$\left. (\omega - \omega^{*'}) J_0^2(x_L') \frac{I_X\left(\tilde{x}_b\ (k',m), \tilde{x}_b\ (k',m'), p\right) e^{ip[\beta_b(k',m) - \beta_b(k',m')]}}{n <\dot{\varphi}>_b - p\omega_b - \omega}\right], \quad (41)$$

using the normalized energy variable $E = \mathcal{E}/v_{th}^2$. In obtaining (41), $\tilde{x}_b \equiv \tilde{x}_b\ (\vec{k})$ has been replaced by $\tilde{x}_b\ (k', m)$ and $\beta_b \equiv \beta_b(\vec{k})$ by $\beta_b(k', m)$, corresponding again to neglecting all drifts in transformation (15), used when going from (18) to (19).

C. Electrons

The contribution from electrons turns out to be significantly simpler than the one from ions. Indeed, for this species, only the non-adiabatic response from the trapped fraction is

taken into account. Furthermore, as the bounce frequency of electrons is high with respect to the frequency of the perturbation, one can in fact consider a bounce-averaged relation [20], consisting in retaining only the contribution of the harmonic $p = 0$ in (19). Finally, FLR as well as finite banana width effects can also be neglected. In this way, as will be shown, one can perform one of the velocity integrals - in this case the integral with respect to energy $\mathcal{E}$ - analytically when evaluating the corresponding density fluctuations, without having to consider the deeply trapped limit as for trapped ions. This approximation is therefore not taken here.

Finite banana width effects being discarded, the Fourier coefficient (9) can thus be evaluated considering only the motion parallel to the magnetic field:

$$
\begin{aligned}
C_0(m; \rho, X) &= \frac{1}{T_b} \int_0^{T_b} dt \exp i \int_0^t dt' k_{\parallel} v_{\parallel} \\
&= \left[\int_{-\theta_b}^{\theta_b} \frac{d\theta}{\sqrt{1 - \lambda(1 - A^{-1}\cos\theta)}} \right]^{-1} \left[\int_{-\theta_b}^{\theta_b} d\theta \frac{e^{i(m-nq_s)\theta}}{\sqrt{1 - \lambda(1 - A^{-1}\cos\theta)}} \right] \\
&= \frac{I_\theta}{2K(X)},
\end{aligned}
\tag{42}
$$

having used $d\theta/dt \simeq -v_{\parallel}/Rq_s$ and with

$$
I_\theta(m; \rho, X) = \int_0^{\theta_b} d\theta \frac{\cos(m - nq_s)\theta}{\sqrt{X - \sin^2(\theta/2)}},
\tag{43}
$$

$$
T_b = \frac{2Rq_s}{\sqrt{\mathcal{E}\lambda A^{-1}}} \int_0^{\theta_b} \frac{d\theta}{\sqrt{X - \sin^2(\theta/2)}} = \frac{4Rq_s}{\sqrt{\mathcal{E}\lambda A^{-1}}} K(X).
\tag{44}
$$

Here, the turning point angle is given by $\theta_b = 2\arcsin\sqrt{X}$ and K stands again for the complete elliptic integral of the first kind. The integrals I_θ can be precalculated numerically, independently of frequency. In the limit $X \ll 1$, it can be easily shown that relation (42) reduces to $C_0 \simeq J_0((m - nq_s)\theta_b)$, in agreement with (39) for zero banana width ($\rho_b = 0$). Inserting relation (42) into (19) gives the contribution to the eigenvalue equation from adiabatic electrons and non-adiabatic trapped electrons:

$$
\begin{aligned}
M_{(k,m),(k',m')}^{electrons} &= \frac{1}{\Delta\rho} \int_{\rho_l}^{\rho_u} d\rho\, e^{-i(k_\rho - k_\rho')\rho} \left(-\frac{Rq_s}{B_0} \frac{Nq^2}{T} \right) [\delta_{m,m'} + \\
&\frac{\sqrt{2A^{-1}}}{2\pi} \int_0^1 dX \lambda\sqrt{\lambda} \frac{I_\theta(m)I_\theta(m')}{K(X)} \frac{1}{\sqrt{2\pi}} \int_0^\infty \frac{d\mathcal{E}\sqrt{2\mathcal{E}}}{v_{th}^3} e^{-\mathcal{E}/v_{th}^2} \frac{\omega - \omega^{*\prime}}{\omega - n <\dot\varphi>_b}],
\end{aligned}
$$

19

where the toroidal precessional drift $<\dot{\varphi}>_b$ is given this time by the full relation (36)- (37). Here the adiabatic term has not been weighted by any fraction, as it stands for both, the circulating and trapped contribution.

The integrals with respect to $\mathcal{E}$ can be expressed in terms of the plasma dispersion function $W(z)$ [21]:

$$W(z) = \frac{1}{\sqrt{2\pi}} \int_{-\infty}^{+\infty} \frac{x}{x-z} \exp(-\frac{x^2}{2}) dx \quad , \quad \Im m(z) > 0.$$

This is carried out as follows, with $E = \mathcal{E}/v_{th}^2$:

$$\frac{1}{\sqrt{2\pi}} \int_0^\infty dE \sqrt{2E} \frac{e^{-E}}{E - \omega/n<\dot{\varphi}>_{b0}} = \frac{2}{\sqrt{2\pi}} \int_0^\infty dy \frac{y^2 e^{-y^2/2}}{(y+z)(y-z)}$$

$$= \frac{1}{\sqrt{2\pi}} \int_0^\infty dy \left(\frac{y}{y+z} + \frac{y}{y-z} \right) e^{-y^2/2} = W(z)$$

and in the same way:

$$\frac{1}{\sqrt{2\pi}} \int_0^\infty dE \sqrt{2E} \frac{E e^{-E}}{E - \omega/n<\dot{\varphi}>_{b0}} = \frac{\omega}{n<\dot{\varphi}>_{b0}} W(z) + \frac{1}{2},$$

having performed the change of variable $E = y^2/2$ and having been careful with causality when defining:

$$z = \text{sign}(n<\dot{\varphi}>_{b0})\sqrt{2\omega/n<\dot{\varphi}>_{b0}}, \quad \text{with} \quad <\dot{\varphi}>_{b0} = -\frac{v_{th}^2}{R^2\Omega} \frac{q_s}{A^{-1}} G.$$

Using these last relations, the electron contribution finally becomes:

$$M_{(k,m),(k',m')}^{electrons} = \frac{1}{\Delta\rho} \int_{\rho_l}^{\rho_u} d\rho e^{-i(k_\rho - k'_\rho)\rho} \left(-\frac{Rq_s}{B_0} \frac{Nq^2}{T} \right) \left[\delta_{m,m'} - \frac{\sqrt{2A^{-1}}}{2\pi} \int_0^1 dX \lambda\sqrt{\lambda} \frac{I_\theta(m)I_\theta(m')}{n<\dot{\varphi}>_{b0}K(X)} \times \right.$$

$$\left. \left\{ \left[\omega - \omega_N(1 - \frac{3}{2}\eta) \right] W(z) - \omega_N\eta \left[\frac{\omega}{n<\dot{\varphi}>_{b0}} W(z) + \frac{1}{2} \right] \right\} \right]. \tag{45}$$

IV. NUMERICAL METHOD

For the large aspect ratio model described in the previous section and assuming a plasma with one species of ions, the two-dimensional eigenvalue equation in Fourier space (k,m) is of the form (20), with:

$$M^{tot} = M^{circ.ions} + M^{trap.ions} + M^{electrons},$$

the different contributions being given respectively by (30), (41) and (45). The infinite system (20) must still be reduced by identifying the finite number of significant matrix elements $M_{(k,m),(k',m')}$.

1. Radial mode numbers

On the basis that all higher radial mode numbers are averaged out over the FLR of ions, the considered values of k for ion driven modes are such that

$$|k| < k_{max} \qquad \text{with} \qquad k_{max}\frac{2\pi}{\Delta\rho}\lambda_L \equiv k_{\rho\,max}\lambda_L \sim 1,$$

where here $\lambda_L = v_{thi}/\Omega_i$ is the thermal ion Larmor radius. In the case of electron driven modes, such as the trapped electron mode (TEM), higher values of k_{max} may have to be considered.

The integrations over ρ in (30), (41) and (45) are carried out by applying fast Fourier transform (FFT) algorithms to n_ρ equidistant mesh-point evaluations. Due to the factor $e^{-i(k_\rho - k'_\rho)\rho}$ appearing in all these relations, the transform is taken from ρ to $k'' = k - k'$. Consistently, the coupling between the radial mode numbers k and k' is therefore only taken into account if $|k''| = |k - k'| \overset{\sim}{<} n_\rho/2$. The density of the radial mesh and thus the coupling between radial mode numbers must naturally increase with the inhomogeneity of the system.

2. Poloidal mode numbers

Microinstabilities tend to align with the magnetic field lines, thus justifying the gyro-ordering assumption $k_{\parallel}\lambda_L \ll 1$. For fixed toroidal wave number n, the significant poloidal mode numbers are therefore those for which the corresponding mode rational surface $\rho = \rho_m$ ($q_s(\rho_m) = m/n$), lies inside the unstable region. A good estimate of this radial interval, for different types of microinstabilities, is obtained applying simple local stability conditions (see e.g. reference [22]).

3. Harmonics of transit and bounce frequency

To determine which orders of the harmonic decomposition must be taken into account in (29) and (40), one must not only consider the resonant denominators, but also the weight of the numerators corresponding to the bulk response. Thus, the nearest neighbors to the resonant harmonic p_r are retained, where

$$p_r = (k_\| v_\| - \omega_r)/\omega_t \qquad \text{for circulating ions}$$

$$p_r = (n <\dot\varphi>_b - \omega_r)/\omega_b \qquad \text{for trapped ions,}$$

having defined $\omega_r = \Re e(\omega)$. The above relations are evaluated for characteristic values, i.e. typically $k_\| v_\| \sim \omega_t \sim \pm v_{th}/Rq_s$, $n <\dot\varphi>_b \sim -v_{th}k_\theta \lambda_L/R$ and $\omega_b \sim \sqrt{A^{-1}} v_{th}/Rq_s$. In general, one retains $|p - p_r| < \Delta p_{extra}$, with $\Delta p_{extra} \sim 5$ to ensure convergence. The numerators however are dominant for

$$|p| \overset{\sim}{<} x_t \sim k_\perp \rho_t \qquad \text{for circulating ions}$$

$$|p| \overset{\sim}{<} x_b \sim k_\perp \rho_b \qquad \text{for trapped ions,}$$

where $\rho_t \sim q_s\lambda_L$ and $\rho_b \sim q_s\lambda_L/\sqrt{A^{-1}}$ are typical radial excursions of circulating and trapped ions respectively. These last values of p must therefore also be included. The last relations are based on the fact that in absolute value, the Bessel function $J_p(x)$ is a decreasing function of p for $|p| > |x|$.

4. Velocity integrals

For circulating ions, the velocity integrals with respect to $(v_\|, v_\perp)$ in (29) must both be calculated numerically. As already pointed out, the $v_\perp$-integrals can be precalculated, while the $v_\|$-integrals must be evaluated for each new considered frequency ω. For trapped ions, the $\mathcal{E}$-integrals in (41) and for trapped electrons the X-integrals in (45) must also be computed numerically for each new frequency.

Owing to the Maxwellian distribution of equilibrium, the considered velocity space can be reduced to the sphere $\mid \vec{v} \mid \; < v_{max}$ with $v_{max} \sim 4v_{th}$. All the velocity integrations are carried out using an extended trapezoidal rule on equidistant meshes. Concerning the $v_{\parallel}$-integral in (29) and the $\mathcal{E}$-integral in (41), the density of the mesh must be such as to resolve the width of the resonances. This width naturally varies with the considered growth rate $\gamma = \Im m(\omega)$ and becomes very narrow near marginal stability. Usual mesh densities are 10 to 20 points per thermal velocity to ensure convergence of final result to the order of a percent.

5. Solving for the eigenfrequencies

Solving the characteristic equation (21) basically consists in finding the zeros of the analytical function $\det M^{tot}$ in the complex frequency plane. This is carried out using an efficient method devised by Davies [9], based on a higher order Nyquist algorithm. This approach requires the sampling of $\det M^{tot}$ along a closed path in the complex ω plane, until a minimum resolution in the phase of the function is obtained. From this sampling, the eigenfrequencies enclosed by the curve can then be determined with very high accuracy. A practical generalization from circular to non-circular contours is described in reference [1].

The process of sampling $\det M^{tot}$ can easily be implemented on a parallel machine with very little message passing required. Indeed, each processor computes independently the determinant for different values of ω. This has been done on a Silicon Graphics Orion 2000, involving up to eight of its R10000 processors. Average computing time of $\det M^{tot}$ is of the order of 1-2 minutes per frequency and per processor. The number of frequency evaluations required is typically of the order of 8 - 16 per enclosed eigenfrequency.

6. Equilibrium profiles

All the numerical results presented in this paper have been computed using the following equilibrium profiles. For density and temperature, the same type of dependence is chosen:

$$\frac{N(s)}{N_0} = \exp\left(-\frac{a\Delta s_N}{L_{0N}}\tanh\frac{s - s_0}{\Delta s_N}\right), \tag{46}$$

$$\frac{T(s)}{T_0} = \exp\left(-\frac{a\Delta s_T}{L_{0T}}\tanh\frac{s - s_0}{\Delta s_T}\right), \tag{47}$$

where $s = \rho/a$ is the normalized radial variable and $\Delta s_{N,T}$ the radial width over which these profiles vary. The characteristic length of variation $L_{N,T} = |d\ln N, T/d\rho|^{-1}$ is minimum at $s = s_0$ and given by $L_{0N,T}$. For the safety factor, a fourth order polynomial is considered:

$$q_s(s) = q_s(0) + as^2 + bs^3 + cs^4. \tag{48}$$

This choice allows one, for instance, to fix the safety factor on axis $q_s(0)$, on the edge $q_s(1)$ as well as its value $q_s(s_0)$ and shear $\hat{s}\,(s_0)$ at an intermediate point s_0.

V. RESULTS

A. Toroidal wave number scan, benchmarking with PIC code

To validate the spectral code, a toroidal wave number scan was carried out, similar to the one previously computed with a linear, time evolution, PIC code [6]. This PIC approach assumes adiabatic electrons and therefore this approximation was also first taken for obtaining the eigenvalue results. Except for FLR effects, included only to second order, the PIC code has full ion dynamics and therefore provides a useful benchmark of the model derived in Sec.III.

In this case, a TFTR-like deuterium plasma is considered. The magnetic geometry (22) is thus chosen with $B_0 = 3.8\,T$, $R = 2.58\,m$, $a = 0.92\,m$, $q_s(s) = 1.2 + 9.6s^3$. The density profile is of the form (46), with $L_{0N} = 0.74\,m$, $\Delta s_N = 0.26$ and $s_0 = 0.315$. Temperature profiles of the form (47) are identical for ions and electrons, with $T_0 = 1.3\,keV$, $L_{0T} = 0.19\,m$, $\Delta s_T = 0.26$ and $s_0 = 0.315$. For these temperatures, the minor radius contains an average of $a/\lambda_L \simeq 650$ ion Larmor radii. At $s = s_0$, where the logarithmic derivatives are maximum and the modes tend to localize, the relevant parameters for local stability take the values $q_s = 1.5$, $\hat{s} = d\ln q_s/d\ln s = 0.6$, $T_e/T_i = 1.0$, $\epsilon_N = L_N/R = 0.29$, $\eta = L_N/L_T = 4.0$,

$A^{-1} = 0.11$, corresponding to a state well above marginal stability. Let us point out, that the density and temperature dependences are only a fit of those in Ref. [6], where the profiles have been defined with respect to the radial variable $s' \sim \sqrt{\psi}$. Also, for a more effective drive when later including the non-adiabatic trapped electron dynamics, a non-flat electron temperature was considered here, while in Ref. [6] $T_e = 1.3 \, keV$ throughout the plasma. This difference is acceptable, as only the adiabatic response of electrons is considered for this comparison.

Comparing spectral and time evolution results is essentially straightforward. Indeed, asymptotically in time the real frequency ω_r, growth rate γ and wave structure of the PIC simulation must match the eigenfrequency and mode structure of the most unstable eigenmode found with the eigenvalue approach. Figure 2 a.) and b.) show ω_r and γ respectively as a function of the toroidal wave number n for both, the spectral and the time evolution approach. For the spectral results, only the most unstable eigenmode is plotted. All frequencies are normalized with respect to $\omega_{norm} = T_{i0}/eB_0a^2 = 404.2 \, s^{-1}$. Values up to $n \sim 100$ have been computed, showing the ability of dealing with low as well as very high toroidal wave numbers. Notice that for $n \stackrel{\sim}{<} 15$, the real frequency $|\omega_r|$ falls bellow the average ion bounce frequency $< \omega_{bi} > (s = s_0) \sim \sqrt{A^{-1}} v_{th}/Rq_s = 53 \, \omega_{norm}$, so that both the toroidal-ITG and the trapped ion mode (TIM) regime are covered here. These plots show good agreement throughout most of the scan. A shift in the real frequency, appearing at higher values of n, may in part be explained by the time evolution results still containing components of next most unstable eigenmode, as shown explicitly in another comparison [8]. The Fourier analysis in time of the PIC signal, necessary to evidence this effect, was not carried out in this case. However, as shown in Fig.3 for $n = 24$, the relative position of the PIC result with respect to the most unstable eigenfrequencies, backs up this explanation. Also represented in Fig.3 is the closed curve which enabled to identify simultaneously the five most unstable eigenmodes with the higher order Nyquist algorithm.

Different mode structures computed with the spectral code are given in Fig.4. The mode $n = 4$ is typical of a TIM instability. Note the almost slab-like character, with only slight

ballooning and the radial width barely spanning the mode rational surfaces neighboring $q_s(s_0) = 1.5$. The modes $n = 64$ and $n = 96$ are however typical of the toroidal-ITG regime, with a strongly ballooned envelope and the width spanning many mode rational surfaces. The case $n = 24$ is near the transition between the two regimes.

The average radial, poloidal and perpendicular components of the wave vector $\vec{k}$ of the most unstable eigenmode are given, as a function of n, in Fig.5. These values, for a given mode structure ϕ, are respectively evaluated using

$$< k_\rho >^2 = \frac{\sum_{(k,m)} | \hat{\phi}_{(k,m)} \, (k2\pi/\Delta\rho)|^2}{\sum_{(k,m)} | \hat{\phi}_{(k,m)} |^2}, \qquad < k_\theta >^2 = \frac{\int_{\rho_l}^{\rho_u} d\rho \sum_m | \hat{\phi}_m(\rho) \, (m/\rho)|^2}{\int_{\rho_l}^{\rho_u} d\rho \sum_m | \hat{\phi}_m(\rho)|^2},$$

$$\text{and} \quad < k_\perp >^2 \; = \; < k_\rho >^2 + < k_\theta >^2,$$

where $\hat{\phi}_m(\rho) = \sum_k \hat{\phi}_{(k,m)} \, e^{i\kappa\rho}$ is the radial dependence of the poloidal Fourier component m. Other average values, discussed further on, are computed with similar relations. The average poloidal component varies essentially linearly with n, following $< k_\theta > \sim nq_s/s_0 a$. The highest growth rate is reached for $n \simeq 64$, where typically $k_\theta \lambda_L \sim 0.5$. The corresponding mode structure is given in Fig.4 c.). The average radial component shows an approximatively linear variation only for high values of n, in agreement with the local ballooning estimate $< k_\rho > = k_\theta \, \hat{s} <\Delta\theta>$, where $<\Delta\theta >$ is the average poloidal width. For lower toroidal wave numbers, this dependence must ultimately break down as $< k_\rho >$ can never fall significantly bellow $2\pi/2\Delta sa$, with Δs the root mean squared width of the mode. This behavior of $< k_\rho >$ as a function of n had already been pointed out in Ref. [4].

The root mean squared width Δs of the most unstable eigenmode as a function of the toroidal wave number is represented in Fig.6. The width is maximum at the transition between the TIM and toroidal-ITG regime. A fit in the toroidal-ITG regime for $n \geq 24$, following a power law $\Delta s \sim n^\nu$, gives $\nu = -0.489$, which verifies the analytical estimate $\Delta s \sim n^{-1/2}$ in Ref. [23], based on a second order, fluid ballooning calculation.

The mixing length estimate [24] $D_{ML} = \gamma/k_\perp^2$ of the diffusion coefficient as a function of n is given in Fig.7 with a line labeled with circles. The maximum value is reached for $n = 24$,

i.e. near the transition from TIM to toroidal-ITG modes and logically located between the toroidal wave number leading to the largest radial width ($n \simeq 15$) and the one giving rise to the highest growth rate ($n \simeq 64$). The corresponding eigenmode structure appears in Fig.4 b.). The diffusion coefficient $D_{ML} = \gamma(a\Delta s/\pi)^2$ estimated with the average radial width Δs of the mode is also plotted in Fig.7, with a diamond-labeled line. The two estimates for D_{ML} show approximatively the same qualitative dependence of n. These results confirm the one of Ref. [6] and tend to emphasize the importance of accurately resolving the intermediate regime between trapped-ion and toroidal-ITG modes for transport simulations.

B. Effect of non-adiabatic trapped electron dynamics

The toroidal wave number scan described in the previous section has been repeated including non-adiabatic trapped electron dynamics. In this case, the spectrum not only contains ITG-type eigenmodes propagating in the ion diamagnetic direction, but also instabilities with a TEM character propagating in the electron diamagnetic direction. The highest growing eigenfrequency for each direction of propagation is given as a function of n in Fig.8. For comparison, results with only the adiabatic electron response have been reported from Fig.2.

Although the growth rate of the ITG-type mode is enhanced when taking into account non-adiabatic trapped electron dynamics -in this case by a factor of the order 2 over most of the scan-, its character is still predominantly determined by the ions. This is in particular revealed by the role over of the growth rate for $k_\theta \lambda_L \sim 0.5$ at $n \simeq 64$. The TEM however is not affected by FLR effects of ions and its growth rate therefore keeps increasing. Thus, for very short wavelengths, the TEM would be the only one to remain unstable before being itself damped by FLR effects of electrons (which would then have to be taken into account in the calculation). The mode structure in the poloidal plane of the ITG and TEM -type eigenmodes are given in Fig.9 for $n = 4$ and $n = 64$. Note that for both modes, the real frequency ω_r is lower (resp. higher) then the average ion bounce frequency $< \omega_{bi} >$ for $n = 4$

(resp. $n = 64$).

C. Larmor radius scaling of radial width in different regimes

The radial width estimate of the eigenmodes being one of the additional informations provided by a global, versus a local ballooning calculation, a study of the Larmor radius scaling of this width has been carried out in different regimes. These results were computed without taking into account the non-adiabatic response of electrons. The corresponding scans, reported in a log-log scale plot in Fig.10, have been carried out starting from the same plasma as in Sec.V A, by varying the ion and electron temperature T_0 at $s = s_0$ as well as the toroidal wave number n such, that the average poloidal wave component normalized with respect to the Larmor radius, $< k_\theta \lambda_L > \sim n\sqrt{T_0}$, remains constant. All other equilibrium parameters are kept unchanged. This ensures that the relevant parameters for a local ballooning calculation, i.e. q_s, $\hat{s}$, T_e/T_i, ϵ_N, η, A^{-1} and $k_\theta \lambda_L$, are constant and that in this sense one stays in the same regime. Such scans were made in the toroidal-ITG regime for $k_\theta \lambda_L \simeq 0.5$ as well as in the TIM regime for $k_\theta \lambda_L \simeq 0.025$, i.e. starting from point $n = 64$ and $n = 4$ respectively in Fig.2. Also considered was the slab-ITG regime, reached when unbending the torus into a cylinder by taking $R \to \infty$, while holding Rq_s and n/R constant. This naturally removes all trapped particles and also corresponds to taking $x'_t = 0$ in relation (29) for circulating ions, clearly eliminating all toroidal coupling between poloidal mode numbers and the radial coupling due to finite orbit width. The only remaining radial coupling is then provided by the Larmor gyration of ions. In this case, the value $k_\theta \simeq 0.1$ was chosen arbitrarily. Figure 10 clearly shows different scalings in these three different regimes. In the toroidal-ITG case, a fit following a power law of the form $\Delta s \sim \lambda_L{}^\nu$ gives $\nu = 0.514$, which verifies the analytical estimate $\Delta s \sim \lambda_L^{1/2}$ in Ref. [23], leading to Bohm scaling of the diffusion coefficient estimated with $D_{ML} = \gamma(a\Delta s/\pi)^2$. In the slab-ITG case, a fit $\lambda_L{}^\nu$ gives $\nu = 0.957$, clearly reproducing the well-known dependence $\Delta s \sim \lambda_L$, leading to a gyro-Bohm scaling of D_{ML}. For the trapped ion modes, one obtains a fit $\lambda_L^{0.691}$, giving

rise to a scaling intermediate between Bohm and gyro-Bohm.

D. Aspect Ratio Scan

To illustrate the transition between the toroidal-ITG and the slab-ITG regime, an initial toroidal configuration, called full torus, is unbent into a cylinder while following the full unstable spectrum. As mentioned above, this is achieved by increasing the major radius R while holding Rq_s, n/R and a constant, as well as all equilibrium profiles. For this calculation, non-adiabatic trapped electron dynamics have again been neglected. In fact, trapped ion dynamics had not yet been included in the code at the time this study was carried out. This, however, has little effect on the results as the real frequency, in the absolute value, stays above the average ion bounce frequency throughout the scan, so that the effect of the trapped ions remains minor.

The full torus plasma has an inverse aspect ratio $A^{-1} = a/R = 0.18$, its magnetic geometry is given by $B_0 = 1.\,T$, $R = 1.19\,m$, $a = 0.21\,m$ and $q_s(s) = 1.25 + 3s^2$. Density and electron temperatures are flat, the ion (hydrogen) temperature is of the form (47), with $T_{i0} = T_e = 1.\,keV$, $L_{0T_i} = 0.16\,m$, $\Delta s_{T_i} = 0.31$ and $s_0 = 0.5$. At $s = s_0$, where the modes tend to be localized, one thus has the local values: $q_s = 2$, $\hat{s} = 0.75$, $T_e/T_i = 1.0$, $\epsilon_{T_i} = L_{T_i}/R = 0.13$ and $a/\lambda_{Li} = 65$. Here frequencies are normalized with respect to $\omega_{norm} = T_{i0}/eB_0a^2 = 2.27 \cdot 10^4 s^{-1}$. In the initial toroidal configuration, the toroidal wave number takes the value $n = 4$, giving an average normalized poloidal component of the order $k_\theta \lambda_L \simeq nq_s\lambda_L/as_0 = 0.25$. Two particular intermediate states, labeled half torus and quarter torus and having respectively half and quarter inverse aspect ratio of full torus, are considered in the following.

Real frequency ω_r and growth rate γ of the most unstable eigenmode are plotted in Fig.11 as a function of the inverse aspect ratio A^{-1}. The full unstable spectra, at the four particular aspect ratios mentioned above, are given by the left column of frames in Fig.12. One must in fact specify what is meant by full unstable spectrum. As already mentioned, an

increasing number of velocity points are required for integrating the resonant denominator as one approaches marginal stability. In this case, growth rates down to $\gamma \simeq 0.2\,\omega_{norm}$ were considered. In cylinder, the set of slab-ITG instabilities, localized on the different mode rational surfaces, have similar growth rates and form a well packed spectrum. With toroidicity, these modes couple together and there appears an isolated eigenmode whose growth rate increases faster then all other values. Simultaneously, some eigenfrequencies already start to be damped. The prominence of this mode corresponds to the transition to the toroidal-ITG instability and, as can be seen in Fig.12, occurs after quarter torus. This is also reflected by the sharp increase of the growth rate in Fig.11 at $A^{-1} \simeq 0.05$. The highest growth rate is reached near half torus and with even stronger curvature the unstable spectra is limited to the single toroidal-ITG eigenmode whose growth rate also begins to decrease.

Plots in the central column of frames of Fig.12 represent, for increasing toroidicity and most unstable eigenmode, the radial dependence of the poloidal Fourier components. Also indicated are the positions of the mode rational surfaces. Frames on the right-hand side give the corresponding structure in configuration space. In cylinder, the most unstable eigenmode turns out to have poloidal mode number $m = 7$. Quarter torus is the onset of transition where the poloidal modes are already coupled by pairs. At this stage, a second eigenmode takes over and gives rise to the true toroidal-ITG instability of half and full torus, nicely centered at $s = s_0 = 0.5$. Coherent radial structures called 'fingers' have now appeared in the unfavorable curvature region where the mode balloons. Their twisting can easily be explained by the increasing of the safety factor towards the edge and using the constant phase relation $q_s(s)\theta =$const. from ballooning representation.

E. Magnetic shear scan

For this scan, the magnetic equilibrium was chosen such that $B_0 = 1.\,T$, $R = 2.\,m$ and $a = 0.5\,m$, that is approximately the dimensions of the DIII-D tokamak. The local parameters are fixed at $s_0 = 0.4$, which enables realistic safety factor profiles of type (48)

to take many different values of shear at this point. The safety factor itself is held at $q_s(s_0) = 1.5$. Positive shear cases up to $\hat{s}(s_0) = +1$ are obtained by convex combinations of profile $q_s^{\#1}$ (defined by: $\hat{s}(s_0) = +1.$, $q_s(s_0) = 1.5$, $q_s(0) = 1.05$, $q_s(1) = 6.5$) and profile $q_s^{\#2}$ ($\hat{s}(s_0) = 0.$, $q_s(s_0) = 1.5$, $q_s(0) = 2.2$, $q_s(1) = 6.0$), while negative shear configurations are obtained by convex combinations of profile $q_s^{\#2}$ and $q_s^{\#3}$ ($\hat{s}(s_0) = -1.$, $q_s(s_0) = 1.5$, $q_s(0) = 2.5$, $q_s(1) = 6.5$). These three particular profiles are given in Fig.13. The density profile, of the form (46), is defined by $L_{0N} = 0.5\,m$, $\Delta s_N = 0.35$ and $s_0 = 0.4$, while the temperature dependence, equal for ions (hydrogen) and electrons, of the form (47) is given by $L_{0T} = 0.2\,m$, $\Delta s_T = 0.2$, $s_0 = 0.4$ and $T_0 = 2.13\,keV$. Furthermore, fixing the toroidal wave number to $n = 10$, the different local parameters take the values $q_s = 1.5$, $T_e/T_i = 1.$, $\epsilon_N = 0.25$, $\eta_i = \eta_e = 2.5$, $k_\theta \lambda_L = 0.35$, $A^{-1} = 0.1$ and $a/\lambda_L = 106$.

Results were first computed neglecting trapped electrons and ions. In this case, real frequency ω_r and growth rate γ as a function of shear $\hat{s}$ are plotted in Fig.14. Here, frequencies are normalized with respect to $\omega_{Ne} = 3.195 \cdot 10^5\,s^{-1}$ evaluated at $s = s_0$. Different unstable eigenmodes computed with the global code are represented with full lines. Note that, in the absolute value, ω_r never falls bellow the average ion bounce frequency $\omega_b \simeq 0.15\,\omega_{Ne}$, thus validating, a posteriori, the absence of trapped ion dynamics for obtaining these results.

For comparison, the growth rate computed by Dong et al. with a local ballooning approximation [25], is drawn with a dashed line. This local calculation is appropriate for comparison with our global results as it also considers a large aspect ratio with only highly passing ions, the electron response being adiabatic.

The evolution of this spectrum can essentially be explained using the relation for the GC drift frequency [26] in the frame of ballooning representation:

$$\omega_{GC} = -k_\theta v_{dz}(\cos\theta + \hat{s}\,\theta\sin\theta).$$

Thus, for a mode which is not too localized around $\theta = 0$, decreasing shear partly suppresses this toroidal drive. In this respect, a shear scan is similar to the toroidicity scan presented in section V D. Hence, for $\hat{s} < 0.5$ the growth rate of the unstable eigenmode decreases

when lowering shear, to the point where at $\hat{s}= -0.5$ the average value of ω_{GC} is insufficient to sustain the toroidal-ITG instability and the transition to a slab-like regime is induced. Typical for such a state, a whole set of new unstable eigenmodes appear with growth rates of the same order. The roll over of γ at $\hat{s}= 0.5$ results in part from the toroidal drive which has become too strong, as in Fig.11 for configurations with too low aspect ratio.

The attenuation of γ by a factor ~ 4.5 between $\hat{s}= 0.5$ and $\hat{s}= -1.0$, observed in Fig.14 for the global results, is significantly more important then the factor ~ 2.5 over the same interval from the ballooning results. This may be explained by the fact that the ballooning approximation, assuming an interchange-like mode structure, is inappropriate for describing the slab-ITG regime at negative shear and tends to overestimate the instability.

In a second step, non-adiabatic trapped electron dynamics were included. The corresponding results for ω_r and γ appear in Fig.15. Besides containing ITG-type eigenmodes propagating in the ion-diamagnetic direction, the spectrum may now also contain TEM-type eigenmodes propagating in the electron diamagnetic direction. For each direction of propagation, only the eigenmodes which turn out to dictate the highest growth rate during one part or the other of the scan have been followed in Fig.15. Note, that for some of these eigenmodes, $|\omega_r|$ approaches and actually falls bellow the average ion bounce frequency $\omega_b \simeq 0.15\,\omega_{Ne}$ for short intervals of $\hat{s}$, especially for modes 1 and 6, which actually go through a transition from ion diamagnetic to electron diamagnetic propagation. As trapped ion dynamics had still not been included, these calculations are not fully consistent in this sense.

The TEM-type eigenmodes are progressively damped when going to negative shear so that no positive frequency is found at $\hat{s}= -1.0$. This can naturally be explained by the decrease of the average amplitude of the toroidal precessional drift which drives these instabilities, from $< G >_X \simeq 1.2$ at $\hat{s}= +1.$ to $< G >_X \simeq 0.2$ at $\hat{s}= -1.0$ (estimates from Rel.(38))

Throughout the scan, the highest growth rate over all eigenvalues is always determined

by the ITG-type instabilities. Except for the fact that more then one of these eigenmodes are already present at $\hat{s}= +1.0$, the qualitative behavior of this part of the spectrum is quite analogous to the one in Fig.14. Quantitative comparison shows that trapped electron dynamics increases the maximum growth rate for all values of shear. An enhancement factor of ~ 3.0 (respectively ~ 3.4) is measured at $\hat{s}= +1.0$ (respectively $\hat{s}= -1.0$) so that in relative values these particles have a slightly more destabilizing effect at negative shear. Thus the attenuation factor of γ through shear reversal between $\hat{s}\simeq 0.5$ and $\hat{s}= -1.0$ is ~ 4.0 instead of ~ 4.5 with only adiabatic electrons.

The structure of the most unstable eigenmode at $\hat{s}= +1.$ and $\hat{s}= -1.$ appear in Fig.16. At $\hat{s}= -1.$ the mode has essentially lost its ballooning envelope and its radial extent is somewhat diminished compared to $\hat{s}= +1.$, indicating a more slab-like character.

VI. CONCLUSIONS

A new formulation has been derived for solving the full two-dimensional eigenvalue problem of electrostatic microinstabilities in a general tokamak geometry. A Fourier representation, adapted to the curved geometry of the system, provides a useful approach for orbit width and Larmor radius to be taken into account to all orders.

At present, this has been demonstrated in the case of a large aspect ratio geometry with circular, concentric magnetic surfaces. For this model equilibria, a set of additional approximations, mainly considering all circulating ions as highly passing and all trapped ions as deeply trapped, led to a final relation, more tractable for a first numerical implementation. Together with a higher order Nyquist method for identifying the full unstable spectrum, which enabled straightforward implementation on a parallel computer, resolution of the eigenvalue problem could thus be achieved in reasonable computing time.

This first model has been extensively benchmarked against a global, linear, time evolution PIC code [6,7], which contains full ion dynamics, except for FLR effects only retained to second order. In both the TIM and toroidal-ITG regime, very good agreement has been

obtained.

The spectral code has then been applied for various studies, which illustrate some of its unique capabilities. In particular, the full unstable spectrum through different regimes could be followed. For instance, it was shown how the slab-ITG spectrum in cylinder, containing many narrow eigenmodes localized on the different unstable mode rational surfaces, is replaced, when unbending the system into a torus, by a toroidal-ITG spectrum with fewer eigenmodes, but with a large radial width spanning the different mode rational surfaces.

The ability of the global approach to provide estimates of the radial correlation length has also been exploited. In this way, it was found that the radial width of the TIM presents a scaling with respect to the ion Larmor radius, which is intermediate between the gyro-Bohm and Bohm scaling of the slab-ITG and toroidal-ITG respectively. This result is somewhat in opposition to the observation made by Tang and Rewoldt in reference [4], where by artificially reducing the width of the unstable region, it was concluded that the radial extent of the TIM seemed to be significantly affected only by the equilibrium lengths. It may be, that if the width of the unstable region had been increased instead, a maximum width of the eigenmode would have also been obtained as a function of the ion Larmor radius.

Such scaling studies, together with a further result described in this paper, pointing out that the mixing length estimate of the diffusion coefficient reaches its maximum near the transition from the toroidal-ITG to the TIM regime, may be of interest when interpreting results on anomalous transport. Nonetheless, one must be cautious before drawing any quantitative conclusions in this respect, as the present model still neglects some important effects. In particular, shear flows, which may partly break up the large radial coherent structures, should be included in the near future.

The role played by non-adiabatic trapped electron dynamics in ITG-related instabilities has also been analyzed with the global eigenvalue code. The basic effects, previously described with local approaches [27,28], have thus been confirmed. For instance, the removal of the threshold on the ion temperature gradient for the onset of instability, observed for non flat densities (low ϵ_N) and achieved by a transition of the toroidal-ITG to the TEM,

is described in reference [13]. In this paper, it was illustrated how for high toroidal wave numbers the toroidal-ITG is damped due to FLR effects of ions while the TEM keeps on growing. Ultimately this would require taking into account banana width and Larmor radii of electrons.

Following experimental observations of core transport barriers in negative central shear (NCS) discharges [29–31], we have studied the stabilizing effect of negative magnetic shear. Not only does it reduce the growth rate of the toroidal-ITG, but also the radial extension by inducing a transition to a more slab-like mode. In the absence of trapped electron dynamics our global calculations predict a stronger attenuation when going to negative shear then local ballooning calculations [25]. This probably illustrates the problem of applying this representation in a slab-like regime. When considering trapped electron dynamics, these particles destabilize the ITG-type mode for all values of shear. The enhancement factor is however larger for negative values, so that the stabilizing effect of shear is slightly reduced. Anyway, realistic negative magnetic shear alone can only account for the complete suppression of the TEM, but not of the ITG instability and thus is not sufficient to explain the dramatic improvement of confinement in the core of NCS discharges. Experimental results [30] point towards the $\vec{E} \times \vec{B}$ flow shear for being responsible of the full stabilization of these modes.

ACKNOWLEDGMENT

REFERENCES

[1] S.Brunner and J.Vaclavik, Phys.Plasmas **5**, 365 (1998).

[2] J.W.Connor, R.J.Hastie, and J.B.Taylor, Phys.Rev.Lett. **40**, 396 (1978).

[3] R.Marchand, W.M.Tang, and G.Rewoldt, Phys.Fluids **23**, 1164 (1980).

[4] W.M.Tang and G.Rewoldt, Phys.Fluids B **5**, 2451 (1993).

[5] M.Artun, W.M.Tang, and G.Rewoldt, Phys.Plasmas **2**, 3384 (1995).

[6] M.Fivaz, Ph.D. thesis, Ecole Polytechnique Fédérale de Lausanne, Switzerland, thesis 1692, (1997).

[7] M.Fivaz, S.Brunner, G.De Ridder, O.Sauter, T.M.Tran, J.Vaclavik, L.Villard, and K.Appert, accepted for publication in Computer Physics Communications.

[8] S.Brunner, M.Fivaz, J.Vaclavik, K.Appert, and T.M.Tran, in *Theory of Fusion Plasmas, Int.Workshop, Varenna, August 1996* (Editrice Compositori, Società Italiana di Fisica, Bologna, 1997), p.101.

[9] B.Davies, Jour.Comp.Phys. **66**, 36 (1986).

[10] S.E.Parker, W.W.Lee, and R.A.Santoro, Phys.Rev.Lett. **71**, 2042 (1993).

[11] R.D.Sydora, V.K.Decyk, and J.M.Dawson, Plasma Phys.Control.Fusion **38**, A281 (1996).

[12] M.Fivaz, T.M.Tran, K.Appert, J.Vaclavik, and S.E.Parker, Phys.Rev.Lett.**78**, 3471 (1997).

[13] S.Brunner, Ph.D. thesis, Ecole Polytechnique Fédérale de Lausanne, Switzerland, thesis 1701, (1997).

[14] P.J.Catto, Plasma Physics **20**, 719 (1978).

[15] W.D.D'haeseleer, W.N.G.Hitchon, J.D.Callen, and J.L.Shohet, *Flux Coordinates and Magnetic Field Structure* (Springer-Verlag, New York, 1991).

[16] B.Coppi, M.Rosenbluth, and P.Rutherford, Phys.Rev.Lett. **21**, 1055 (1968).

[17] B.B.Kadomtsev and O.P.Pogutse, in *Reviews of Plasma Physics* (M.A.Leontovich, Consultants Bureau, New York, 1970), Vol.5, p.249.

[18] M.Abramowitz, and I.A.Stegun, *Handbook of Mathematical Functions*, (John Wiley & Sons, New York, 1964).

[19] I.S.Gradshteyn and I.M.Ryzhik, *Table of Integrals, Series, and Products* (Academic, New York, 1965).

[20] M.N.Rosenbluth, Phys.Fluids **11**, 869 (1968).

[21] B.D.Fried and S.D.Conte, *The Plasma Dispersion Function* (Academic, New York, 1961).

[22] J.W.Connor and H.R.Wilson, Plasma Phys.Control.Fusion **36**, 719 (1994).

[23] F.Romanelli and F.Zonca, Phys.Fluids B **5**, 4081 (1993).

[24] B.B.Kadomtsev, *Plasma Turbulence* (Academic, London and New York, 1965)

[25] J.Q.Dong, Y.Z.Zhang, S.M.Mahajan, and P.N.Guzdar, Phys.Plasmas **3**, 3065 (1996).

[26] W.Horton Jr., Duk-In Choi, and W.M.Tang, Phys.Fluids **24**, 1077 (1981).

[27] F.Romanelli and S.Briguglio, Phys.Fluids B **2**, 754 (1990).

[28] G.Rewoldt and W.M.Tang, Phys.Fluids B **2**, 318 (1990).

[29] F.M.Levinton, M.C.Zarnstorff, S.H.Batha, M.Bell, R.E.Bell, R.V.Budny, C.Bush, Z.Chang, E.Fredrickson, A.Janos, J.Manickam, A.Ramsey, S.A.Sabbagh, G.L.Schmidt, E.J.Synakowski, and G.Taylor, Phys.Rev.Lett. **75**, 4417 (1995).

[30] L.L.Lao, K.H.Burrell, T.S.Casper, V.S.Chan, M.S.Chu, J.C.DeBoo, E.J.Doyle, R.D.Durst, C.B.Forest, C.M.Greenfield, R.J.Groebner, F.L.Hinton, Y.Kawano, E.A.Lazarus, Y.R.Lin-Liu, M.E.Mauel, W.H.Meyer, R.L.Miller, G.A.Navratil, T.H.Osborne, Q.Peng, C.L.Rettig, G.Rewoldt, T.L.Rhodes, B.W.Rice, D.P.Schissel, B.W.Stallard, E.J.Strait, W.M.Tang, T.S.Taylor, A.D.Turnbull, R.E.Waltz, and the DIII-D Team, Phys.Plasmas B **3**, 1951 (1996).

[31] Y.Neyatani and the JT-60 Team, Plasma Phys.Control.Fusion **38**, A181 (1996).

FIGURE CAPTIONS

Fig.1 Magnetic coordinate system (ψ, χ, φ) in a general axisymmetric system.

Fig.2 Real frequency ω_r (a) and growth rate γ (b) along a toroidal wave number scan for a TFTR-like plasma. Here, the non-adiabatic response of electrons is not taken into account. The most unstable eigenfrequency obtained with the spectral code for each value of n is plotted with a circle. Results given by the linear, PIC code are marked with crosses. For $n \lesssim 15$, $|\omega_r|$ falls bellow the average ion bounce frequency, which corresponds to a transition from the toroidal-ITG to the TIM regime.

Fig.3 Five most unstable eigenfrequencies (circles) of spectrum in the case $n = 24$ of Fig.2. The closed curve used for applying the higher order Nyquist algorithm is represented with a dashed line. Real frequency and growth rate of the PIC simulation are added with a cross. One sees good agreement between the two methods on the growth rate. The difference with respect to ω_r may in part be explained by the PIC signal still containing some contributions from the next most unstable eigenmodes.

Fig.4 Eigenmode structures in the poloidal plane for $n = 4$ (a), $n = 24$ (b), $n = 64$ (c) and $n = 96$ (d) of Fig.2. Dash-dotted lines correspond to mode rational surfaces $s = 0.2$ and $s = 0.4$. The case $n = 4$ is typical of a TIM mode, i.e. barely spanning three consecutive mode rational surfaces and only slightly ballooned. The eigenmode $n = 24$ is near the transition between the toroidal-ITG and the TIM regime and gives rise to the highest value of the mixing length estimate $D_{ML} = \gamma/k_\perp^2$. The eigenmodes $n = 64$ and $n = 96$ are typical of the toroidal-ITG regime: strong ballooning and radially oriented, coherent structures spanning many mode rational surfaces. The case $n = 64$ corresponds to the highest growth rate, while $n = 96$ is already attenuated due to FLR effects.

Fig.5 Average perpendicular (circles), poloidal (diamonds) and radial (squares) wave components, normalized with respect to the ion Larmor radius, for the scan of Fig.2. For

high toroidal wave numbers, $< k_\rho >$ and $< k_\theta >$ vary essentially linearly with n. This breaks down in the case of $< k_\rho >$ for low values of n, due to the finite radial extension of the system.

Fig.6 Root mean squared radial width Δs of the most unstable eigenmode along the n-scan of Fig.2. The maximum width is reached at the transition between the toroidal-ITG and TIM regime. For the toroidal-ITG modes, Δs basically varies as $1/\sqrt{n}$.

Fig.7 Mixing length estimate D_{ML} of the diffusion coefficient for the scan of Fig.2. Both, the average perpendicular wave component $< k_\perp >$ (circles) and the average radial width Δs (diamonds) were used for estimating D_{ML}. The maximum values are reached near the transition from the toroidal-ITG to the TIM regime.

Fig.8 Real frequency ω_r (a) and growth rate γ (b) along the toroidal wave number scan of Fig.2 having taken into account non-adiabatic trapped electron dynamics. The spectrum now contains modes propagating in the ion, as well as in the electron diamagnetic direction. The most unstable eigenmode for each direction of propagation have been plotted with diamonds and squares respectively. As a reference, results from Fig.2 with only the adiabatic electrons have been plotted with circles.

Fig.9 Eigenmode structures relative to results from Fig.8 including non-adiabatic trapped electron dynamics. Modes propagating in the ion diamagnetic direction for $n = 4$ and $n = 64$ are given in frames (a) and (b) respectively. Modes propagating in the electron diamagnetic direction for $n = 4$ and $n = 64$ are given in frames (c) and (d) respectively.

Fig.10 Scaling of the radial width Δs with the ion Larmor radius in different regimes. These results were computed considering only the adiabatic response of electrons. The toroidal-ITG (squares) and slab-ITG (circles) regimes basically show a dependence as $\Delta s \sim \sqrt{\lambda_L}$ resp. $\Delta s \sim \lambda_L$, leading respectively to a Bohm resp. gyro-Bohm scaling of

the mixing length estimate D_{ML}. For the TIM regime (stars) an intermediate scaling is found.

Fig.11 Real frequency ω_r (a) and growth rate γ (b) of highest growing eigenmode when going from cylinder to a toroidal configuration called full torus, having an inverse aspect ratio $A^{-1} = a/R = 0.18$. At quarter torus ($A^{-1} \simeq 0.05$) a sharp increase in the growth rate corresponds to the transition from the slab- to the toroidal-ITG regime.

Fig.12 Unstable spectra (left frames), radial dependence of poloidal mode components (central frames) and mode structure in poloidal plane (right frames) of most unstable eigenmode in cylinder (a), quarter torus (b), half torus (c) and full torus (d). The dash-dotted lines in the frames on the right are the magnetic surfaces $s = 0.2, 0.4, \ldots, 1$.

Fig.13 Safety factor profiles with fixed value $q_s = 1.5$ and shear $\hat{s} = +1$ (dashed line), $\hat{s} = 0$ (full line), $\hat{s} = -1$ (dash-dotted line) at $s_0 = 0.4$

Fig.14 Real frequencies ω_r (a) and growth rates γ (b) as a function of shear $\hat{s}$, without non-adiabatic trapped electron dynamics. Results obtained by following different eigenmodes using the global eigenvalue code are plotted with full lines. With decreasing shear, the toroidal mode (1) becomes slab-like and new eigenmodes (2, 3, & 4) appear. The growth rate of the local ballooning approximation results are reproduced with a dashed line.

Fig.15 Real frequencies ω_r (a) and growth rates γ (b) as a function of shear $\hat{s}$, taking into account non-adiabatic trapped electron dynamics. For $\hat{s} = +1.0$ the unstable spectrum contains simultaneously positive and negative frequencies, corresponding to modes having a TEM respectively an ITG character. At $\hat{s} = -1.0$ only the ITG-type modes remain destabilized, however, with a significantly reduced growth rate compared with the highest one around $\hat{s} = +0.5$.

Fig.16 Mode structure of the highest growing eigenmode for $\hat{s} = +1.$ and $\hat{s} = -1..$ These

results have been computed with non-adiabatic trapped electron dynamics.

FIG.1 Brunner
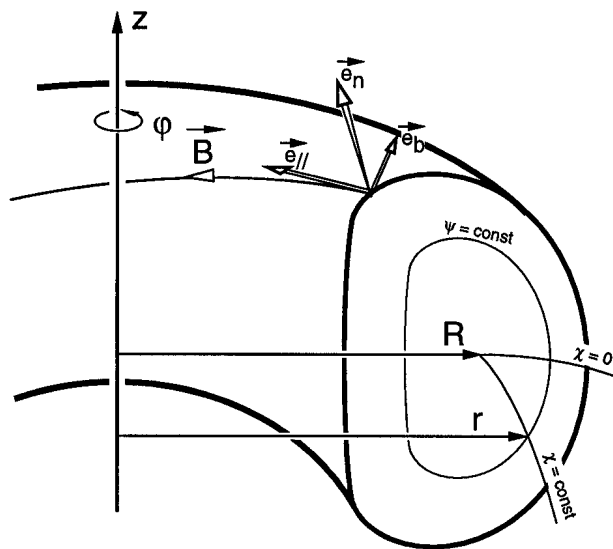
FIG.2 Brunner
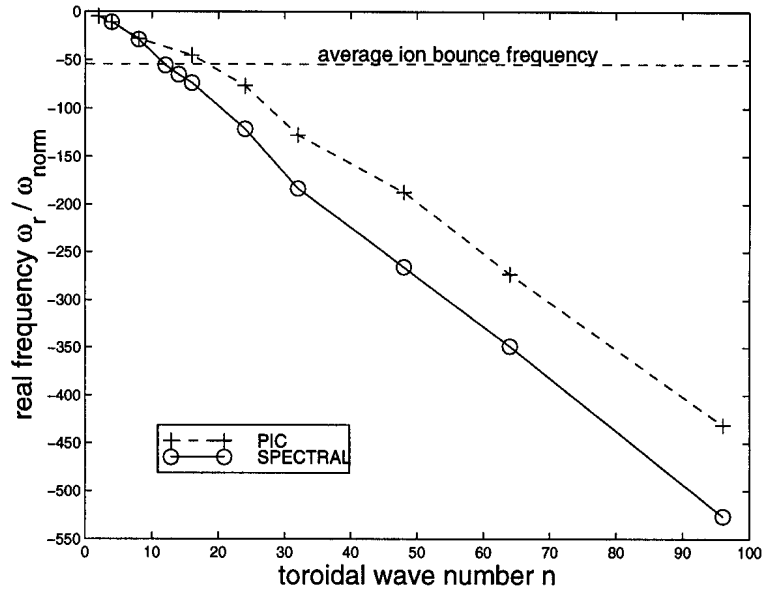
a.)
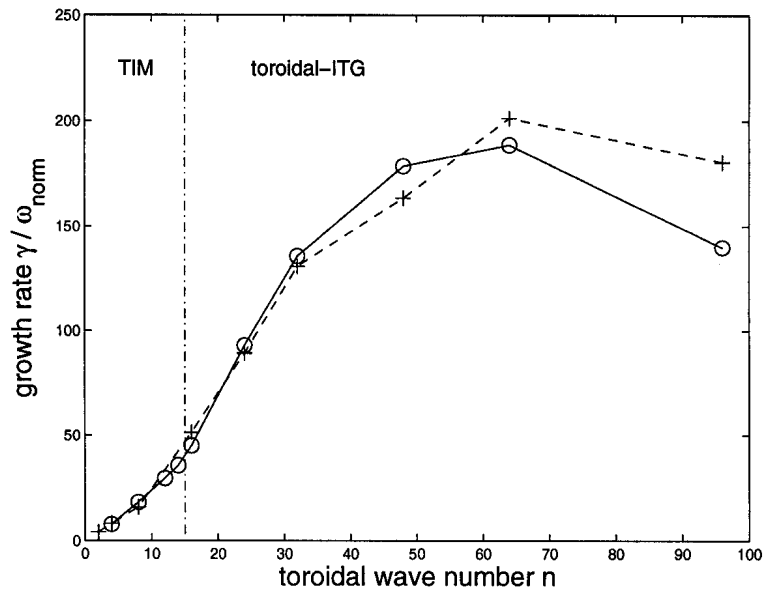
b.)

FIG.3 Brunner
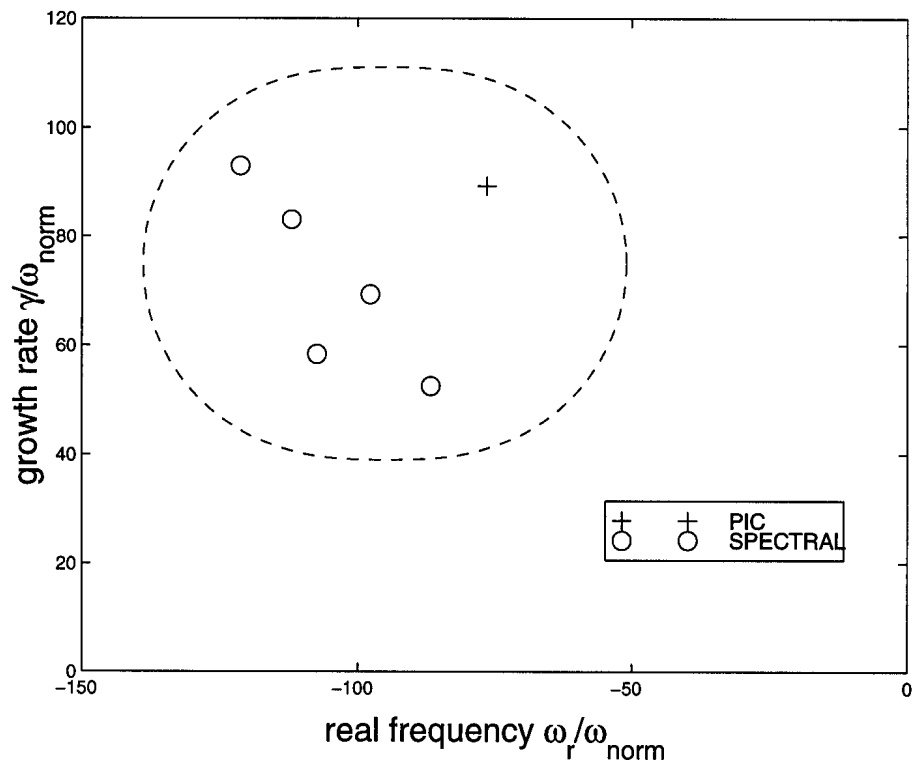
FIG.4 Brunner
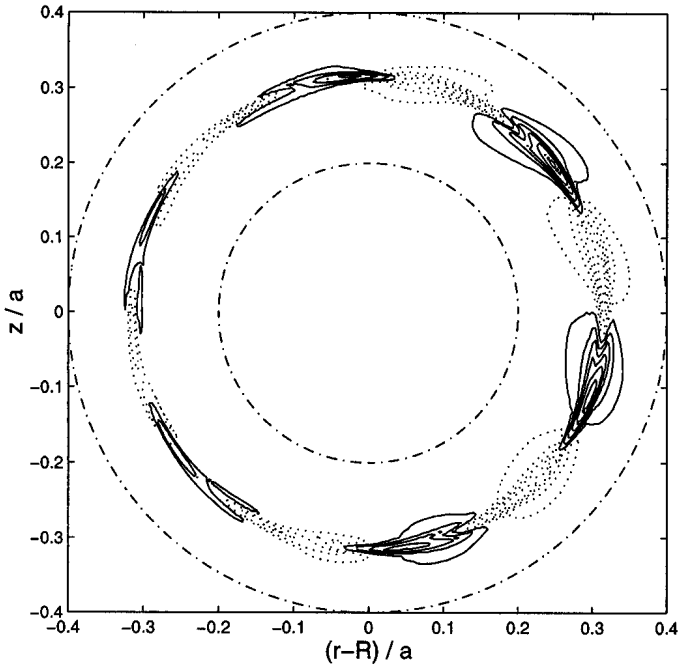
a.) $n = 4$
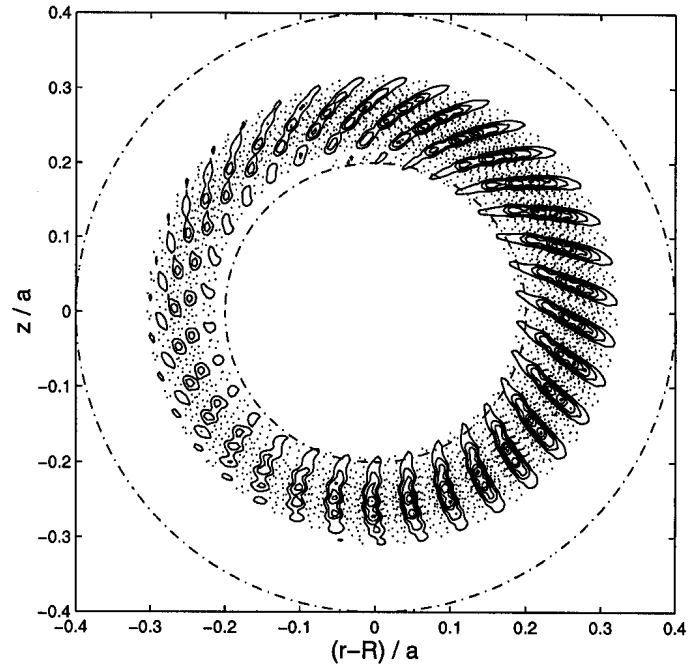
b.) $n = 24$
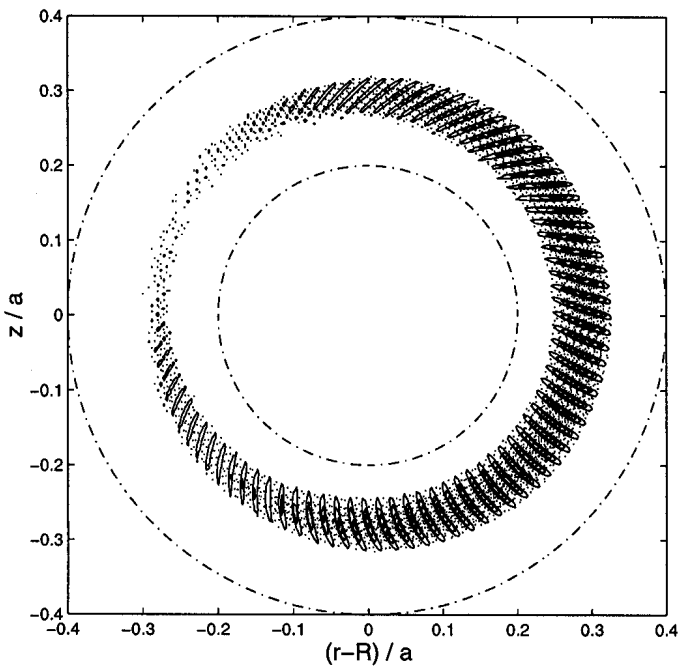
c.) $n = 64$
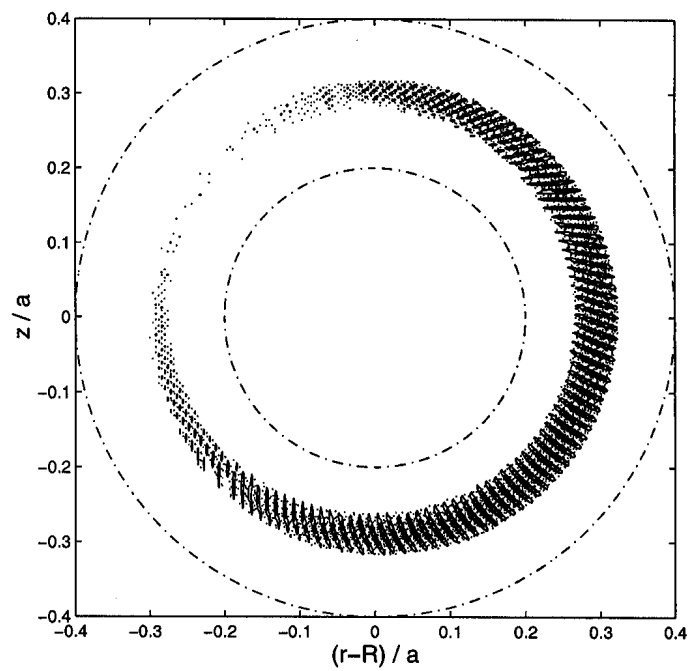
d.) $n = 96$

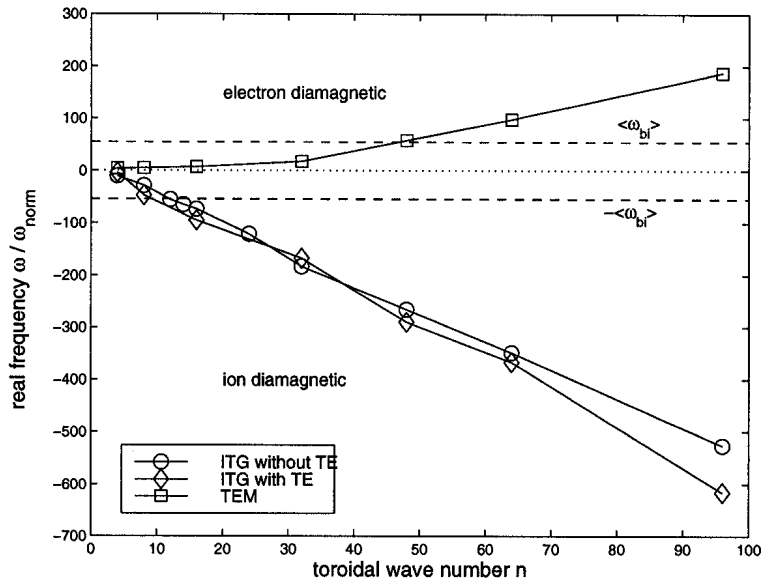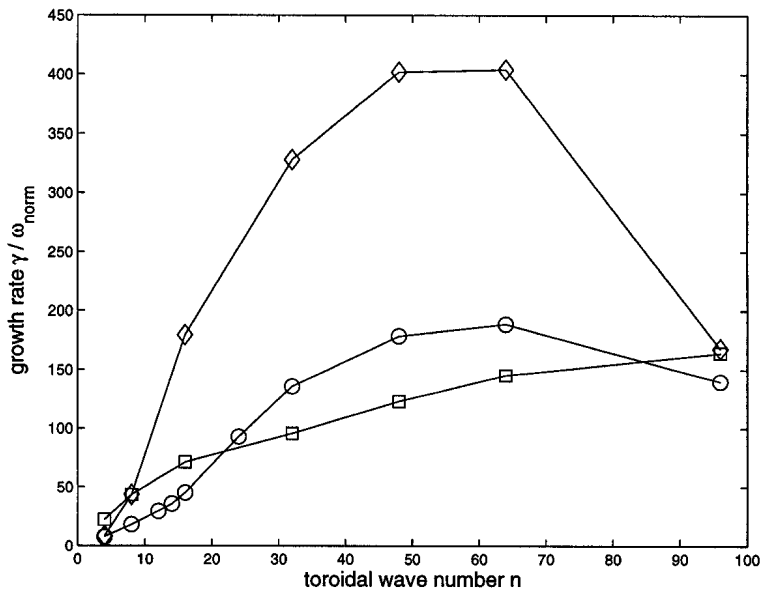**FIG.5 Brunner**
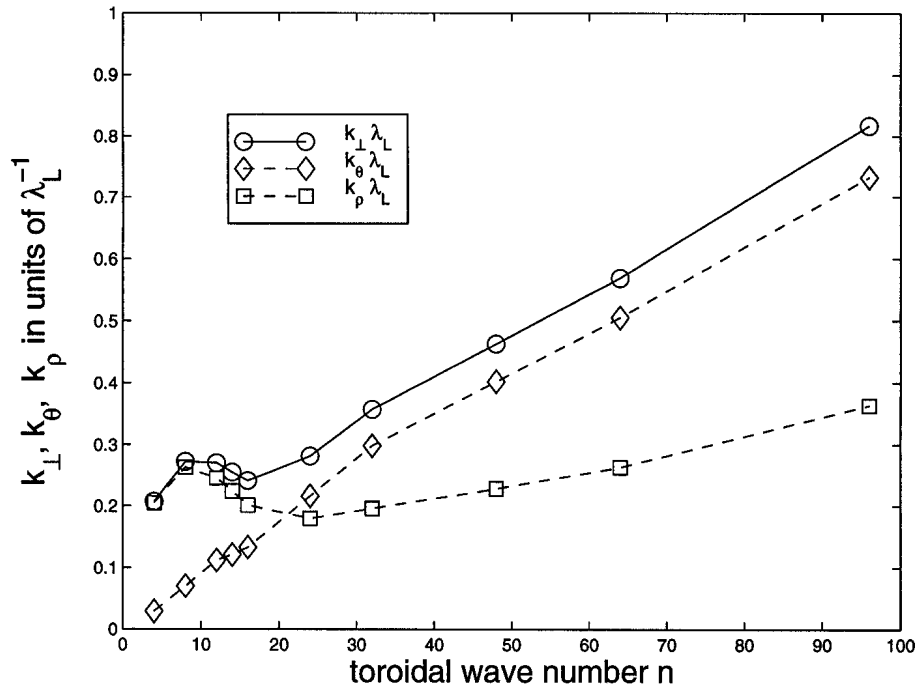
FIG.6 Brunner
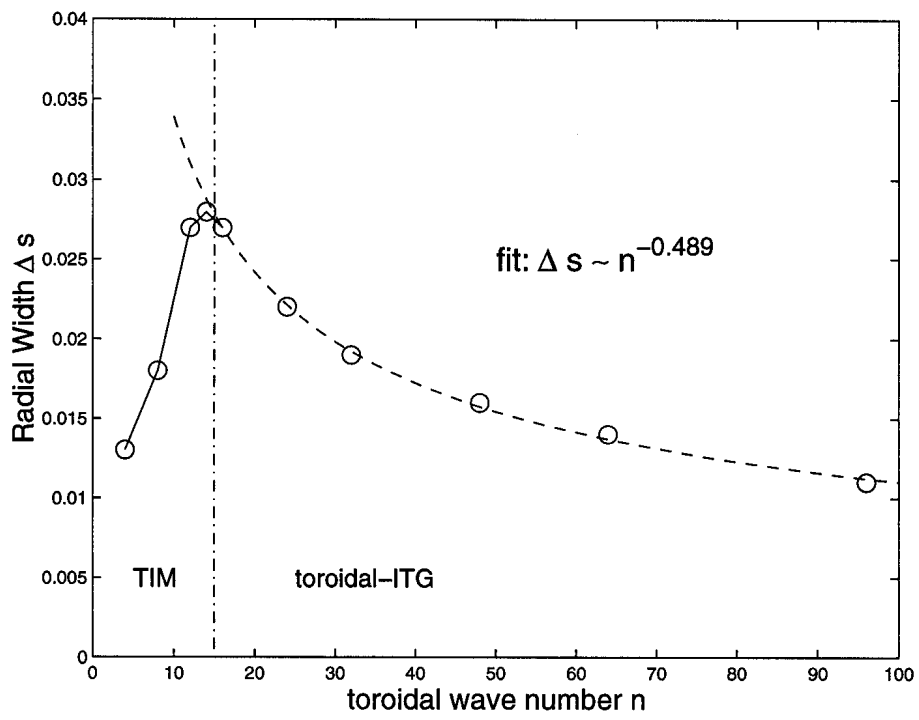
FIG.7 Brunner
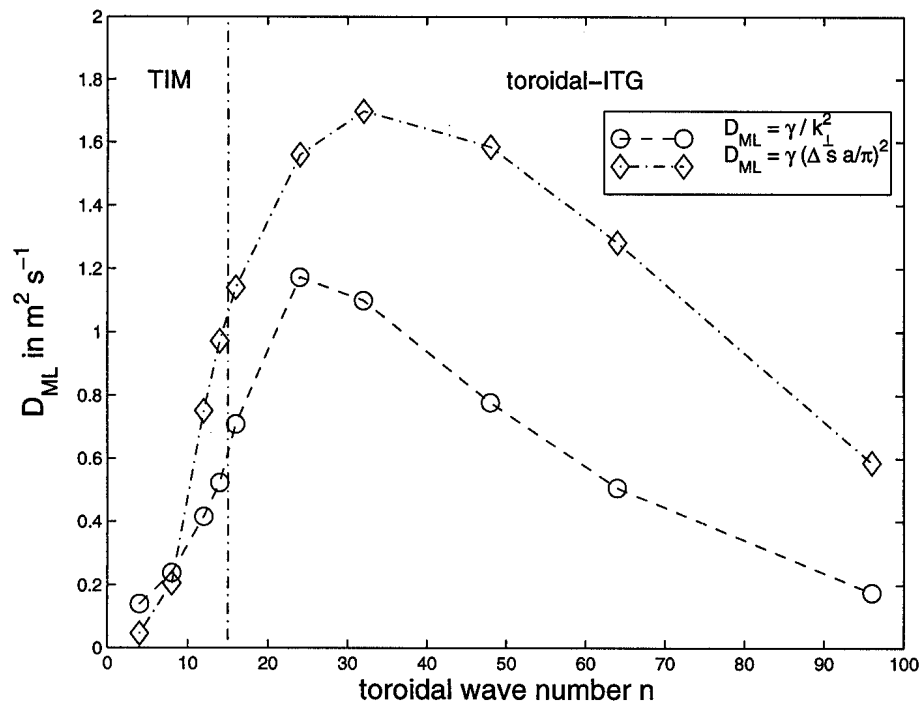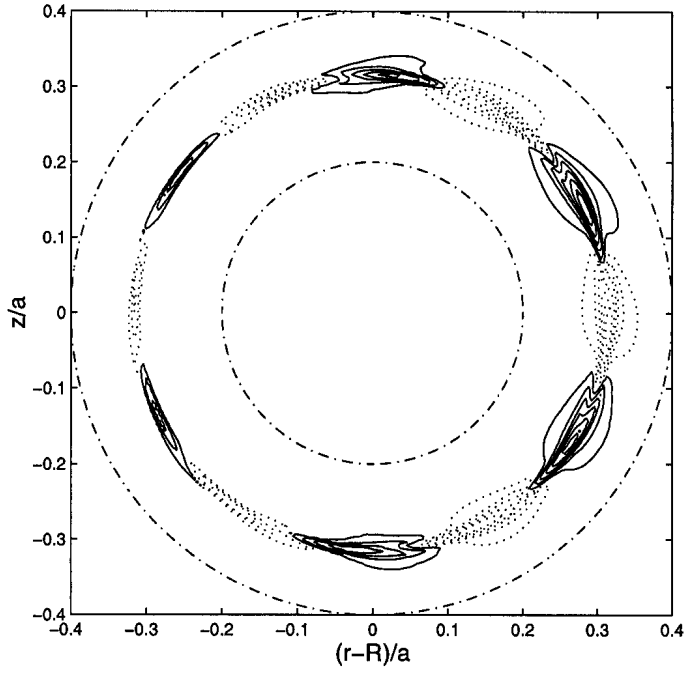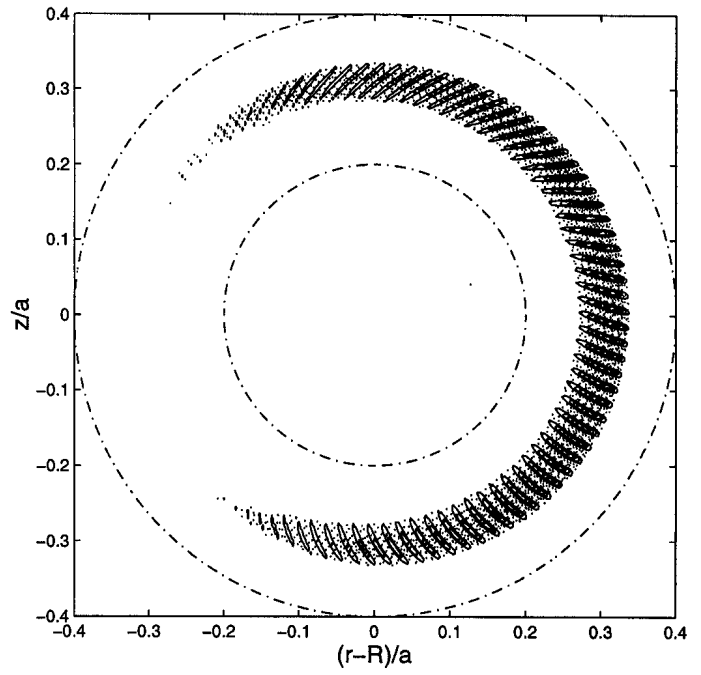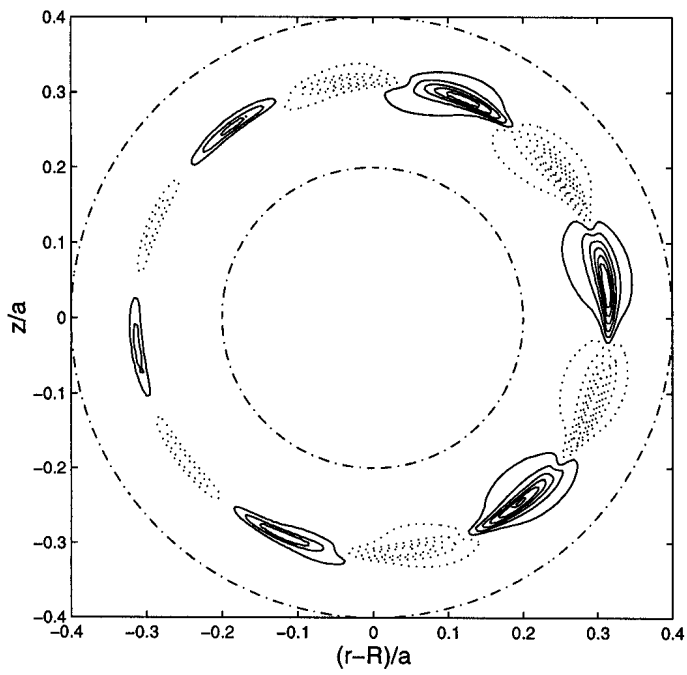
FIG.8 Brunner

a.)

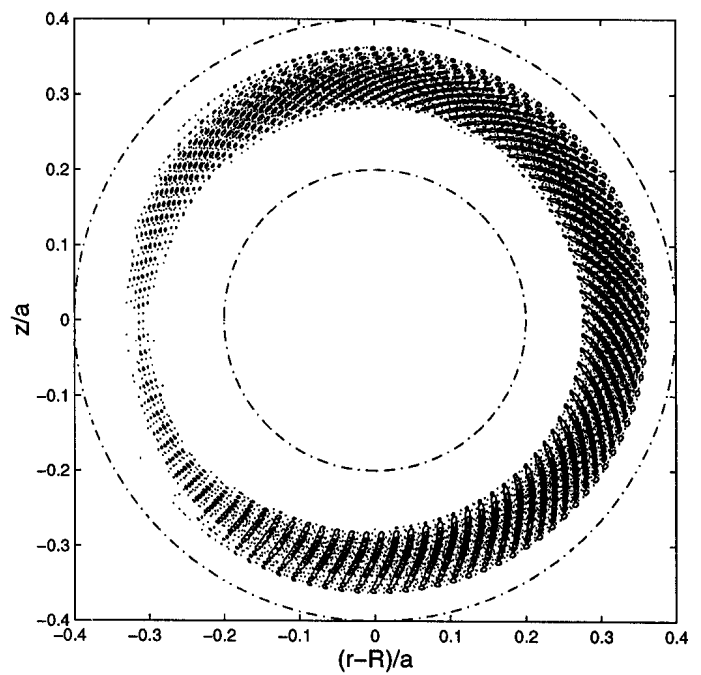b.)

FIG.9 Brunner

a.) ITG $n = 4$

b.) ITG $n = 64$

c.) TEM $n = 4$
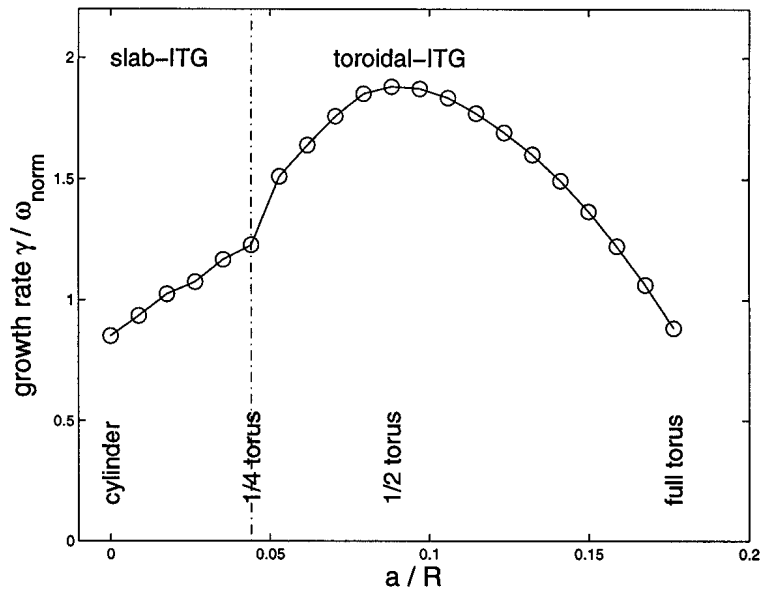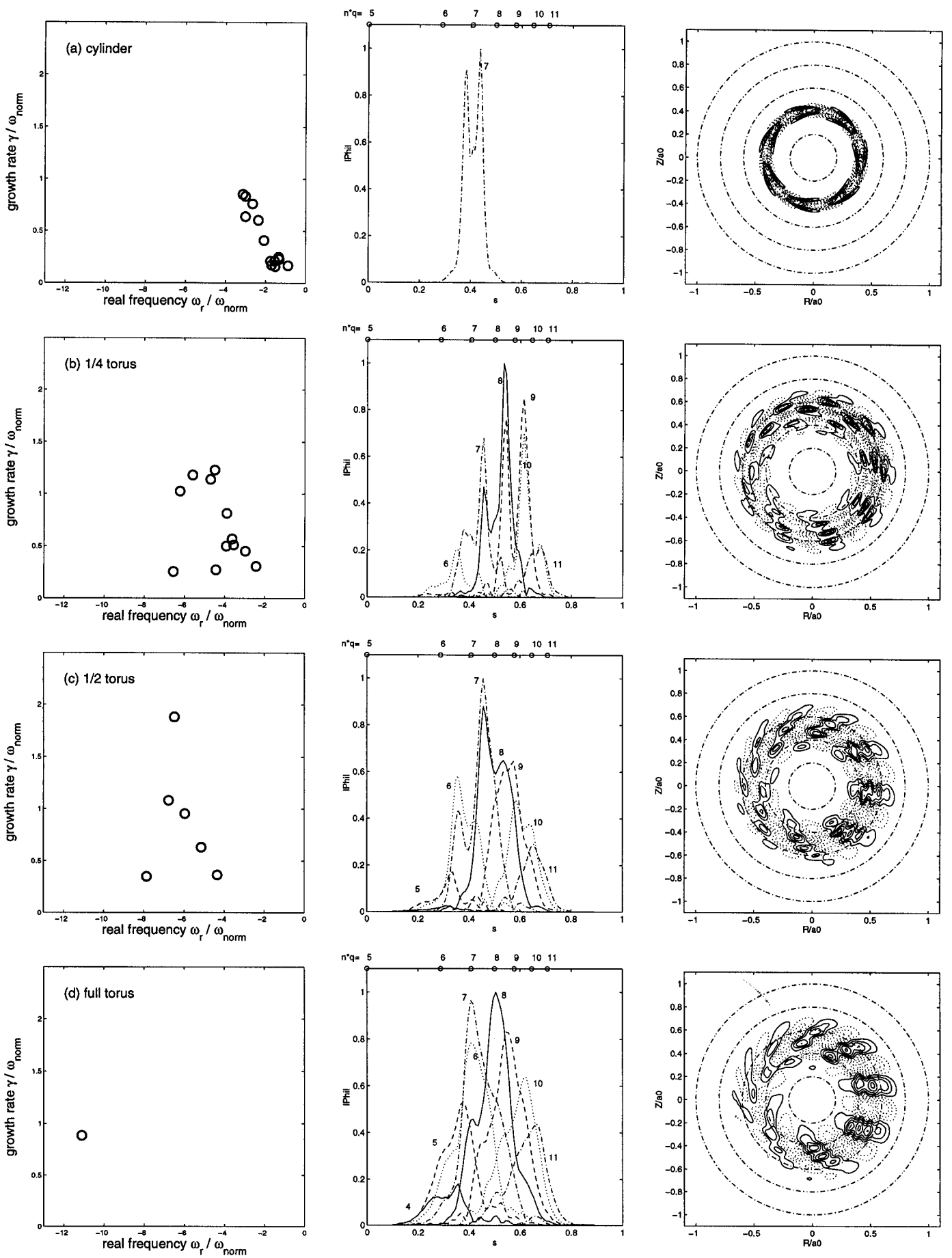

d.) TEM $n = 64$

FIG.10 Brunner

slab-ITG fit: $\Delta s \sim \lambda_L^{0.957}$

TIM fit: $\Delta s \sim \lambda_L^{0.691}$

toro-ITG fit: $\Delta s \sim \lambda_L^{0.514}$
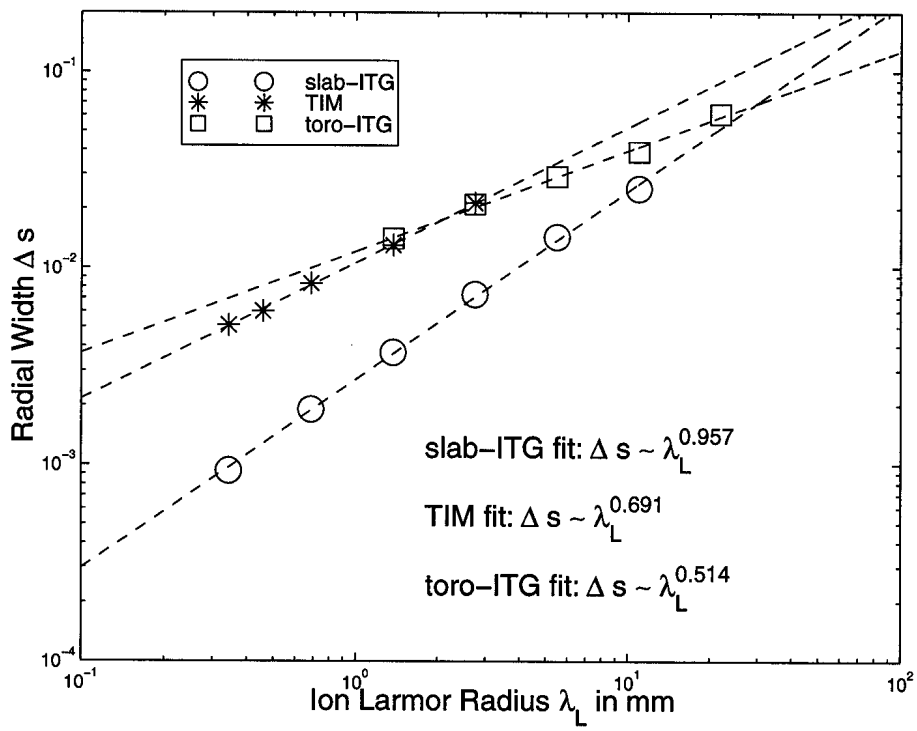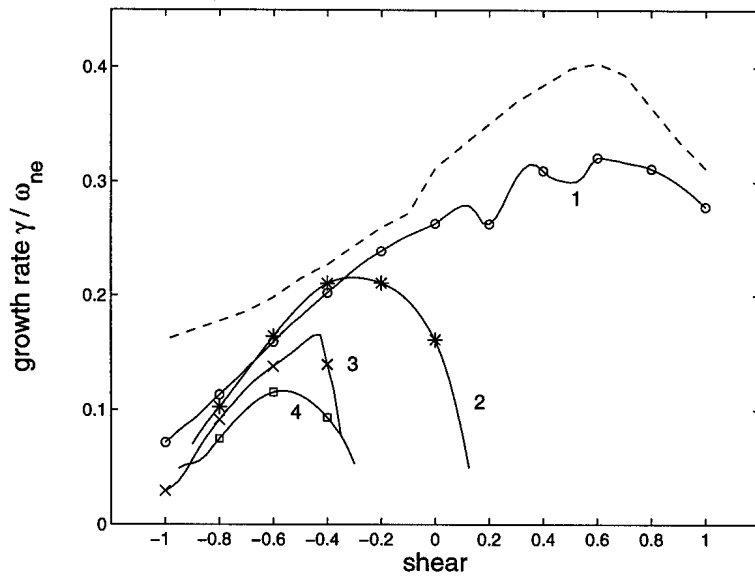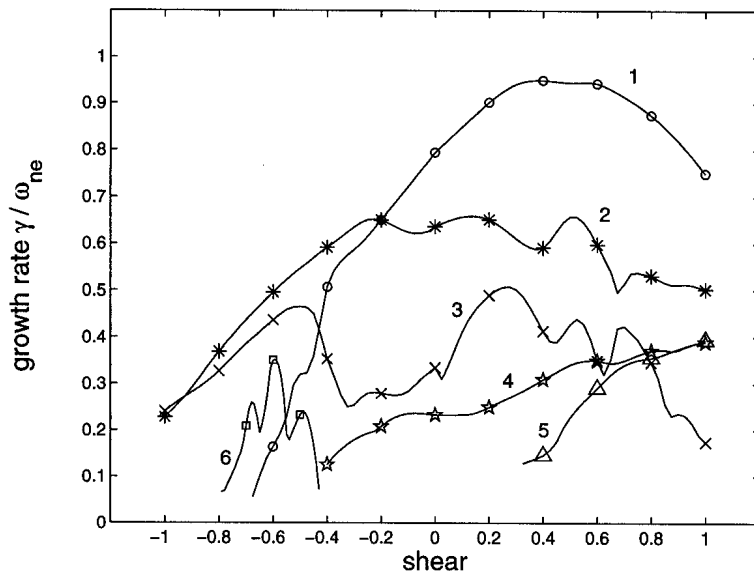
FIG.11 Brunner
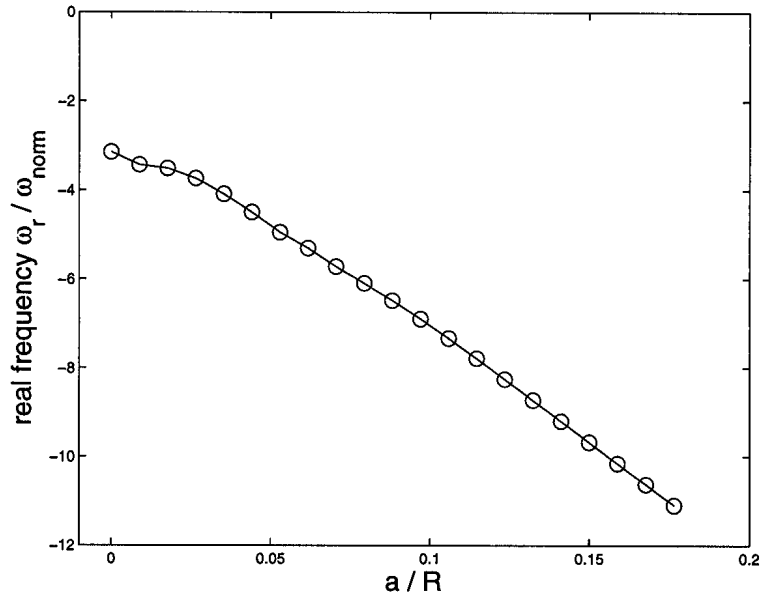
a.)

b.)

FIG.12 Brunner

FIG.13 Brunner
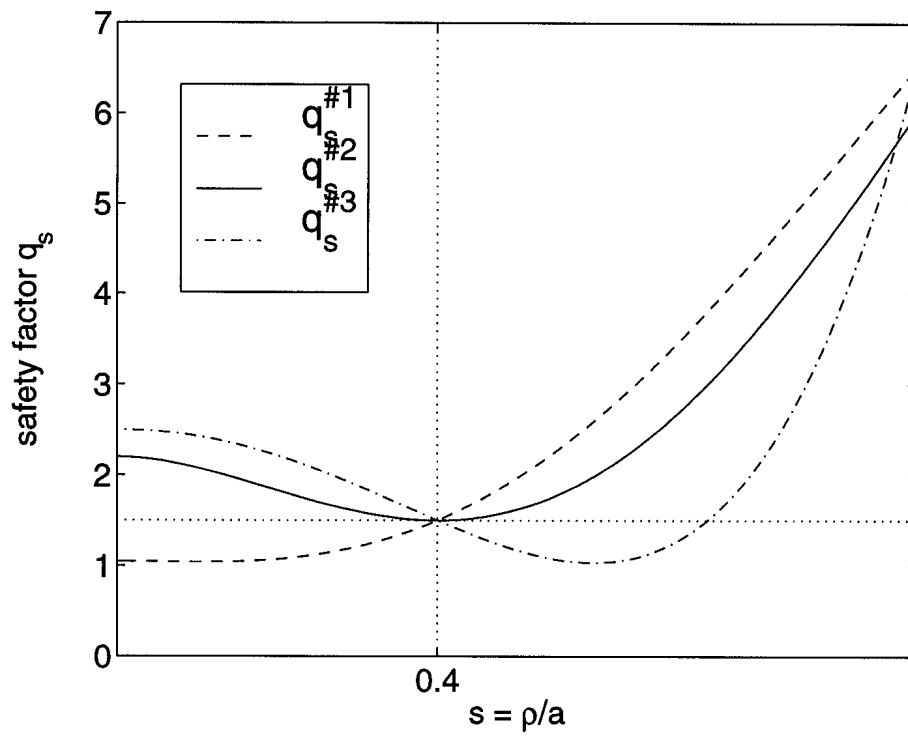
FIG.14 Brunner

a.)

b.)

FIG.15 Brunner

a.)

b.)